Surface Reflection: Physical and Geometrical Perspectives

Shree K. Nayar, *Member, IEEE,* Katsushi Ikeuchi, *Member, IEEE,* and Takeo Kanade, *Senior Member, IEEE*

Abstract—**Machine vision can greatly benefit from the development of accurate reflectance models. There are two approaches to the study of reflection: physical and geometrical optics. While geometrical models may be construed as mere approximations to physical models, they possess simpler mathematical forms that often render them more usable than physical models. However, in general, geometrical models are applicable only when the wavelength of incident light is small compared to the dimensions of the surface imperfections. Therefore, it is incorrect to use these models to interpret or predict reflections from smooth surfaces; only physical models are capable of describing the underlying reflection mechanism.**

In this paper, reflectance models based on physical optics and geometrical optics are studied in detail. More specifically, we consider the Beckmann–Spizzichino (physical optics) model and the Torrance–Sparrow (geometrical optics) model. We have chosen these two particular models as they have been reported to fit experimental data well. Each model is described in detail, and the conditions that determine the validity of the model are clearly stated. By studying reflectance curves predicted by the two models, we propose a reflectance framework comprising three components: the diffuse lobe, the specular lobe, and the specular spike. The effects of surface roughness on the three primary components are analyzed in detail.

Index Terms—**Beckmann–Spizzichino model, electromagnetic waves, geometrical optics, machine vision, physical optics, primary reflection components, radiometry, surface reflection, surface roughness, Torrance–Sparrow model, unified reflectance framework.**

I. Introduction

POINTS in a scene, when illuminated, reflect incident light in various directions. Light rays that are reflected in the direction of the sensor cause an image of the scene to be formed. Most machine vision problems involve the analysis of images formed in this manner. The intensity at any given point in the image is closely related to the reflectance properties of the corresponding point in the scene. Therefore, the prediction or the interpretation of image intensities requires a sound understanding of the various mechanisms involved in the reflection process. While algorithms for recovering information from images are being developed and refined, it is also essential to research and utilize more sophisticated reflectance models.

Manuscript received August 30, 1990; revised January 15, 1991. This work was conducted at the VASC Center at Carnegie-Mellon University and was supported by Westinghouse Electric Corporation and by DARPA under Contract F33615–87–C-1499.

S. K. Nayar is with the Department of Computer Science, Columbia University, New York, NY 10027.

K. Ikeuchi and T. Kanade are with The Robotics Institute, Carnegie-Mellon University, Pittsburgh, PA 15213.

IEEE Log Number 9100897.

A. Reflectance Models in Vision

Various reflectance models have been used in the area of machine vision. Broadly speaking, these models can be classified into two categories: diffuse reflectance models and specular reflectance models. Horn [11] used the Lambertian model [19] for diffuse reflectance to develop shape-from-shading algorithms. He has also provided an excellent review of some of the early models used for hill shading in computer graphics [13]. The Lambertian model was also used by Woodham [40] to determine object shape by means of photometric stereo. This idea was extended by Coleman and Jain [6] who proposed the four-source photometric stereo. They discard specular reflections and use diffuse reflections and the Lambertian model to determine shape information. Phong [25] proposed a parametrized continuous function to represent specular reflectance and used it to render images of objects. Ikeuchi [17] used the double-delta specular model to determine the shape of specular surfaces by photometric stereo. The same model was later used by Sanderson *et al.* [29] to determine the shape of specular surfaces by means of the structured highlight technique. More recently, Nayar *et al.* [21] developed the photometric sampling method that uses a hybrid reflectance model, comprised of both Lambertian and specular models, to extract the shape and reflectance of surfaces.

The above applications have proven that the Lambertian model does reasonably well in describing diffuse reflection. Moreover, its simple functional form has made it a popular reflectance model in the vision research community. On the other hand, the specular models used in the past provide reasonable approximations only when the object surface is very smooth (mirror-like), in which case most of the reflected light is concentrated in the specular direction. Specular reflection from rough surfaces, however, requires careful examination. Its dependence on the imaging and illumination geometry can only be determined by a formal treatment of optics. There are two different approaches to optics, and thus two different approaches to the study of reflection. The physical optics approach uses electromagnetic wave theory to analyze the reflection of incident light. The geometrical optics approach, on the other hand, uses the short wavelength of light to simplify the analysis of the reflection problem. Hence, reflectance models derived using geometrical optics are approximations to those derived using physical optics.

The Beckmann–Spizzichino physical optics model and the Torrance–Sparrow geometrical optics model have recently attracted considerable attention. Both models have been developed to describe specular reflection mechanisms, and both have been found to fit experimental data well [16], [38]. Owing to its simpler mathematical form, the Torrance–Sparrow model is more popular than the Beckmann–Spizzichino model and has been used in the areas of vision and graphics. Healey and Binford [10] used the Torrance–Sparrow model to determine local shape from specular reflections. The model was also used by Wolff [39] to develop spectral and polarization stereo methods. Cook and Torrance [7] modified the model and used it to render images of objects. Tagare and deFigueiredo [35] have discussed both the Beckmann–Spizzichino and the Torrance–Sparrow models in their survey of various reflection mechanisms. They have also used the Torrance–Sparrow model to recover the shape and reflectance of surfaces [36].

B. Motivation

Geometrical reflectance models are more widely used in machine vision than physical reflectance models.[1] This is because geometrical models have simpler mathematical forms and hence are easier to use. This simplicity results from the basic assumption underlying geometrical optics; the wavelength of incident light is assumed to be much smaller than the dimensions of the reflecting surface's irregularities. In the case of smooth surfaces, however, irregularities are often comparable to the wavelength of incident light. In such cases, geometrical reflectance models are generally not valid, and only reflectance models based on physical optics are capable of describing the underlying reflection mechanisms.

The physical optics approach uses electromagnetic wave theory to describe the reflection process. This formulation of the reflection problem is very precise. However, it is often difficult to obtain a closed-form solution to the problem. Hence, like geometrical reflectance models, physical reflectance models are also derived by making certain assumptions. These assumptions are generally related to the electrical properties of the surface. It is important to note that the assumptions made by the two approaches are different. Physical reflectance models are applicable to surfaces that vary from perfectly smooth to very rough. In that respect, physical models are more general, and the assumptions used by them are not as restrictive as those used by geometrical models.

The purpose of this paper is twofold. First, we compare reflectance models based on both geometrical optics and physical optics. We feel that a detailed understanding of the two different approaches would be valuable to machine vision researchers. In particular, we study the Beckmann–Spizzichino physical optics model and the Torrance-Sparrow geometrical optics model. These two models were chosen as they have been found to fit experimental data well [16], [38]. The main steps in the derivations of the two models are described and the assumptions made during the derivations are clearly stated. This part of the paper may be viewed as a tutorial.

Next, both models are used to predict the reflectance of surfaces with different roughness values. Reflectance plots produced by the two models are carefully studied to identify the main reflection mechanisms. We then propose a reflectance framework that is comprised of three primary components; the diffuse lobe, the specular lobe, and the specular spike. This framework describes the reflection of monochromatic light from surfaces that vary from smooth to rough.

Reflection is closely related to the microscopic shape of the surface. In the following section, we describe two methods of modeling surface shapes. In Section III, we highlight the main steps that are involved in the derivations of the Beckmann–Spizzichino and Torrance–Sparrow models. After each model is derived, the assumptions used by the model are listed and discussed. In Section IV, we compare the two models on the basis of reflectance plots produce by them and we identify the primary components of reflection. Finally, we present the unified reflectance framework and describe how reflectance models used by existing photometric methods fall within this framework.

II. Modeling Surfaces

The manner in which light is reflected by a surface is dependent on, among other factors, the microscopic shape characteristics of the surface. A smooth surface, for instance, may reflect incident light in a single direction, while a rough surface tends to scatter light in various directions, maybe more in some directions than others. To analyze the reflection of incident light, we must know the microscopic shape of the reflecting surface, i.e., we need a mathematical model of the surface. All possible surface models may be divided into two broad categories: surfaces with exactly known profiles and surfaces with random irregularities. An exact profile may be determined by measuring the height at each point on the surface by means of a sensor such as the *stylus profilometer* [2]. This method, however, is cumbersome and also inapplicable in many practical situations. Hence, it is often convenient to model a surface as a random process. The surface is described by a statistical distribution of either its height with respect to a certain mean level or its slope with respect to its mean (macroscopic) slope. In this section, we describe the height distribution model and the slope distribution model.

A. Height Distribution Model

The height coordinate h of the surface may be expressed as a random function of the coordinates x and y, as shown in Fig. 1. The shape of the surface is then determined by the probability distribution of h. For instance, let h be normally distributed, with mean value $\langle h \rangle = 0$, and standard deviation σ_h. Then, the distribution of h is given by:

$$\rho_h(h) = \frac{1}{\sqrt{2\pi}\sigma_h} e^{-\frac{h^2}{2\sigma_h^2}}. \tag{1}$$

The standard deviation σ_h is also the root-mean-square of h and represents the *roughness* of the surface. The surface is not

[1] We refer to reflectance models derived using geometrical optics and physical optics as geometrical reflectance models and physical reflectance models, respectively. Both geometrical and physical reflectance models are, however, based on the laws of physics.

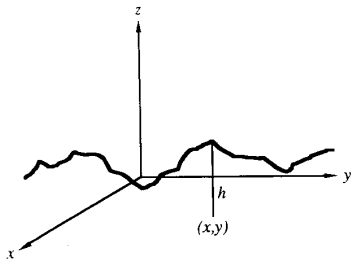

Fig. 1. Surface height as a random function of the spatial coordinates.

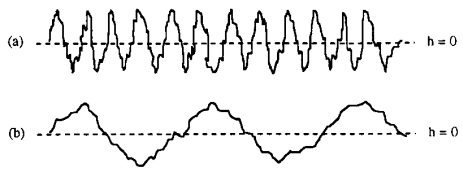

Fig. 2. Random surfaces with (a) small and (b) large correlation distances.

completely defined by the statistical distribution of h, however, as it does not tell us anything about the distances between the hills and valleys of the surface. In Fig. 2, both surfaces (a) and (b) have the same height distribution function, i.e., the same mean value and standard deviation. In appearance, however, the two surfaces do not strongly resemble each other. In order to strengthen the surface model, we use an autocorrelation coefficient $C(\tau)$ that represents the correlation (or lack of independence) between the random values assumed by the height h at two points (x_1, y_1) and (x_2, y_2), separated by a distance τ. The autocorrelation coefficient may be represented, for instance, by the function:

$$C(\tau) = e^{-\frac{\tau^2}{T^2}} \tag{2}$$

where T is the *correlation distance,* for which $C(\tau)$ drops to the value e^{-1}. The surfaces (a) and (b) shown in Fig. 2 have small and large correlation distances, respectively. By varying the parameters σ_h and T of the surface model, the appearance of the surface can be altered. Moreover, if we are dissatisfied with the performance of the model, some other height distribution function and/or autocorrelation function can be used instead of the ones given above.

B. Slope Distribution Model

It is sometimes convenient to think of a surface as a collection of planar micro-facets, as illustrated in Fig. 3. A large set of micro-facets constitutes an infinitesimal surface patch. The patch has a mean normal vector $\boldsymbol{n}$, whereas each micro-facet in the patch has its own normal vector that may deviate from the mean normal by an angle α. We refer to α as the slope of the micro-facet. The profile of the surface patch may be modeled by assuming α to be a random variable. If the surface is isotropic, the probability distribution of α is rotationally symmetric with respect to the mean surface normal $\boldsymbol{n}$. Then the distribution of α can be expressed as a one-dimensional function. For instance, α may have a normal

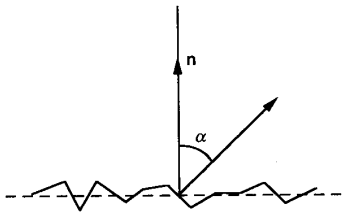

Fig. 3. Surface modeled as a collection of planar micro-facets.

distribution with mean value $<\alpha>= 0$ and standard deviation σ_α:

$$\rho_\alpha(\alpha) = \frac{1}{\sqrt{2\pi}\sigma_\alpha} e^{-\frac{\alpha^2}{2{\sigma_\alpha}^2}}. \tag{3}$$

The surface model in this case is determined by a single parameter, namely, σ_α, unlike the height distribution model which requires two parameters. Larger values of σ_α are used to model rougher surfaces. The advantages of using a single parameter come with the cost of a weaker model when compared to the height model. Given a probability distribution function for σ, it is difficult to visualize the shape of the surface and to estimate the root-mean-square height of the surface. However, the slope distribution model is popular in the analysis of surface reflection, as the scattering of light rays is found to be dependent on the local slope of the surface and not the local height of the surface. Hence, the slope model, though relatively ambiguous, is more directly applicable to the problem of surface reflection. In the following section, both the height and slope models described in this section are used to develop surface reflection models.

III. Surface Reflection

When light is incident on a boundary interface between two different media, it is reflected according to well-known laws. The reflection of light by a surface can be studied using optics. There are two approaches to optics, and thus two approaches to the study of reflection. *Physical* or *wave* optics is based directly on electromagnetic wave theory. It uses Maxwell's equations to study the propagation of light. *Geometrical* or *ray* optics, on the other hand, explains the gross behavior of light when its wavelength is small compared to the pertinent physical dimensions of the system (in our case, the surface irregularities).

In this section, we study surface reflection from the perspectives of physical and geometrical optics. More specifically, we discuss a physical optics reflectance model, namely, the Beckmann–Spizzichino model, and a geometrical optics reflectance model, namely, the Torrance–Sparrow model. We highlight the main steps that are involved in the derivations of both models and clearly state the assumptions made in the process of their development. The derivations will draw on the surface modeling methods discussed in the previous section. In the next section, the two models are compared by plotting the predicted reflectance as functions of viewer and source directions.

A. Physical Optics Model

Light is an electromagnetic phenomenon. In physical optics, problems related to the propagation of light are analyzed using electromagnetic wave theory. In the case of reflection, the interaction between incident light waves and the surface material is described using Maxwell's equations. A reflectance model is then derived by solving Maxwell's equations using the boundary conditions imposed by the reflecting surface.

In this section, we describe the development of the Beckmann–Spizzichino physical optics reflectance model. The model is derived using basic concepts of electromagnetic wave theory. A brief tutorial on electromagnetic waves is given in Appendix A. A reader unfamiliar with this area is encouraged to read Appendix A before proceeding further.

1) Beckmann–Spizzichino Model: The Beckmann–Spizzichino model describes the reflection of plane electromagnetic waves from smooth and rough surfaces. A detailed derivation of this model can be found in [1]. Our intention is to highlight the key steps involved in the derivation of the model and to clearly state the assumptions made during its development.

Consider a plane wave incident on a surface, as shown in Fig. 4. All vectors and surface points are defined using the Cartesian coordinates x, y, z with origin O and unit vectors $\boldsymbol{x}, \boldsymbol{y}$, and $\boldsymbol{z}$. The height of the surface is determined by the function $h = h(x, y)$, and the mean level of the surface is the plane $z = 0$. The location of a surface point Q is given by its displacement vector $\boldsymbol{r}$:

$$\boldsymbol{r} = x\boldsymbol{x} + y\boldsymbol{y} + h(x, y)\boldsymbol{z}. \tag{4}$$

All quantities associated with the incident field will be denoted by the subscript 1 and all those associated with the scattered field by the subscript 2. The plane wave is represented by its electric field intensity. Note that its magnetic field intensity can be determined from the electric field. The incident field at the surface point Q may be written as:

$$\boldsymbol{E} = E_{o1}\boldsymbol{e}_1 e^{-i\boldsymbol{k}_1 \cdot \boldsymbol{r}} e^{i\omega t} \tag{5}$$

where E_{o1} represents the electric field amplitude, $\boldsymbol{e}_1$ is the direction of the electric field, $\boldsymbol{k}_1$ is the wave propagation vector, and ω is the radian frequency of field oscillation.

We are interested in the instantaneous scattering of the incident plane wave by the surface. Hence, the second exponential term in the above equation can be dropped as it represents the temporal variation of the incident field. The incident propagation vector $\boldsymbol{k}_1$ will be assumed to always lie in the $x - z$ plane of the coordinate frame. The angle of incidence θ_i of the plane wave is the angle between the propagation vector $\boldsymbol{k}_1$ and the z axis of our coordinate frame. If we are interested in the field scattered by the surface in the direction $\boldsymbol{k}_2$, the corresponding scattering angle θ_r is the angle between $\boldsymbol{k}_2$ and the z axis. For scattering directions that lie outside the *plane of incidence* $(\boldsymbol{k}_1, \boldsymbol{z})$, an additional angle ϕ_r, must be introduced (Fig. 4). The propagation constant k corresponding to the propagation vectors $\boldsymbol{k}_1$ and $\boldsymbol{k}_2$ is related to the wavelength λ of the incident wave (Appendix A).

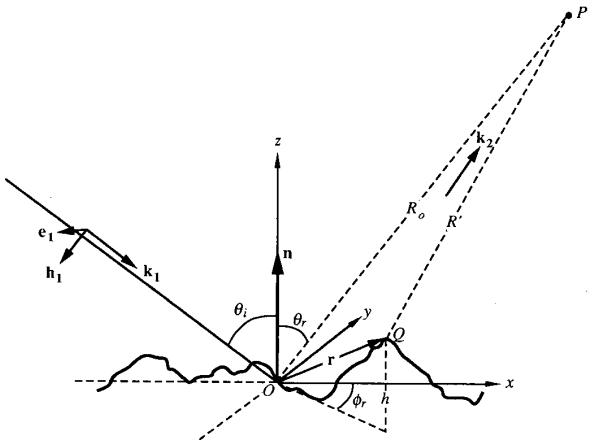

Fig. 4. Plane wave incident on a rough surface.

The polarization of the incident wave is determined by the direction of the vector $\boldsymbol{e}_1$. For parallel polarization, $\boldsymbol{e}_1$ lies in the plane of incidence; for perpendicular polarization, $\boldsymbol{e}_1$ is normal to the plane of incidence. For an unpolarized incident wave, the direction of $\boldsymbol{e}_1$ can vary with time. Here, we assume the polarization of the incident wave to be either parallel or perpendicular. The incident field is denoted by the scalar E_1, where

$$E_1 = \boldsymbol{e}_1 \cdot \boldsymbol{E}_1. \tag{6}$$

What happens when the incident plane wave strikes the surface? A simplistic description of this physical situation is as follows. Consider the electrons in the surface that are loosely bound to their atoms. When these electrons are subjected to the electromagnetic field carried by the incident wave, they experience forces. These forces results in movement of the electrons, often referred to as surface currents. The surface currents give rise to new electromagnetic fields that interact with the incident field to determine the resultant field at the surface. Mathematically, the resultant field $(E)_S$ at a surface point Q must satisfy the *wave equation*[2]:

$$\Delta^2(E)_S + k^2(E)_S = 0 \tag{7}$$

where k is once again the propagation constant. Therefore, the field $(E)_S$ at the surface may be determined by solving the wave equation for the boundary conditions imposed by the surface shape.

The field scattered by the surface in any direction can be determined from the field at the surface. Let P be the point of observation, and let the variable R' denote the distance between P and points on the surface S, as shown in Fig. 4. We are interested in the scattered field E_2 at the point P. To this end, consider a volume V that is bounded almost everywhere by the surface S but is extended such that the point P lies just outside V. Then, it is reasonable to assume that the field E_S is continuous, and the above wave equation

[2]It can be shown [4] that, for a source-free region of space, Maxwell's equations reduce to the wave equation.

must therefore be satisfied everywhere inside V. Furthermore, the point inside V that is nearest to P will experience almost the same field as P. Using these assumptions and Green's first and second theorems, the scattered field E_2 at the point P can be determined [1] from (7) as:

$$E_2(P) = \frac{1}{4\pi} \iint \left((E)_S \frac{\partial \psi}{\partial n} - \psi \left(\frac{\partial E}{\partial n} \right)_S \right) dS \qquad (8)$$

where

$$\psi = \frac{e^{ikR'}}{R'}. \qquad (9)$$

This is called the *Helmholtz integral*. It gives the solution of the wave equation at any point inside (P is almost inside) a region in terms of the values of the function (surface field $(E)_S$) and its normal derivative on the boundary (the surface S) of the region. A detailed derivation of the Helmholtz integral is provided in [1].

In order to evaluate the above integral, we must find $(E)_S$ and $(\partial E/\partial n)_S$, i.e., the field and its normal derivative on the surface S. In general, these two quantities are unknown. *Kirchoff's assumption* may be used to approximate the values of the field and its normal derivative at each point on the surface. The approximation is obtained by assuming that the surface does not have any sharp (compared to the wavelength of incident light) edges, and thus the field at a point on the surface is equal to the field that would be present on a tangent plane at that point. Under this assumption, the field on S may be determined as:

$$(E)_S = (1 + F)E_1. \qquad (10)$$

In addition, by differentiating this equation, the normal derivative of the field is determined as:

$$\left(\frac{\partial E}{\partial n} \right)_S = (1 - F)E_1 \boldsymbol{k}_1 \cdot \boldsymbol{n}' \qquad (11)$$

where $\boldsymbol{n}'$ is the normal to the surface at the point under consideration and F is the *Fresnel reflection coefficient*.

The Fresnel coefficient determines the fraction of incident field that is reflected by a smooth surface. Though the surface we have considered may be rough, Kirchoff's approximation implies that the surface is locally smooth. Therefore, the Fresnel coefficient is applicable. We now take a closer look at how the Fresnel coefficient is related to the electrical properties of the reflecting surface. Consider a plane wave incident on a perfectly smooth surface. A fraction of the incident energy is reflected by the surface and the remaining energy transmitted by the surface. As described above, the intensity of the reflected wave is determined by the surface field $(E)_S$, which in turn is dependent on the surface currents. The surface currents induced by the incident wave are determined by the angle of incidence, the polarization of the incident wave, and the electrical properties (permittivity, permeability, and conductivity). The Fresnel reflection coefficient F is the fraction of incident field that is reflected. It is often written as $F(\theta_i', \eta')$, where θ_i' represents the angle of incidence, and η' is the *complex index of refraction* whose value is determined by the electrical properties of the surface medium. In deriving their reflectance model, Beckmann and Spizzichino have assumed that the incident wave is of either perpendicular or parallel polarization. The Fresnel coefficients for parallel and perpendicular polarization are, respectively [1]:

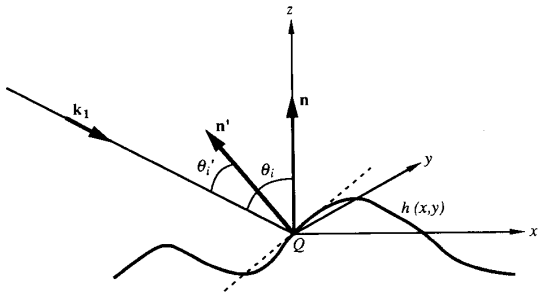

Fig. 5. The local scattering geometry. The local angle of incident θ_i' and the local surface orientation $\boldsymbol{n}'$ may differ from the global angle of incidence θ_i and the mean surface orientation $\boldsymbol{n}$.

$$F_{\text{para}} = \frac{Y^2 \cos\theta_i' - \sqrt{(Y^2 - \sin^2\theta_i')}}{Y^2 \cos\theta_i' + \sqrt{(Y^2 - \sin^2\theta_i')}} \qquad (12)$$

$$F_{\text{perp}} = \frac{\cos\theta_i' - \sqrt{(Y^2 - \sin^2\theta_i')}}{\cos\theta_i' + \sqrt{(Y^2 - \sin^2\theta_i')}}. \qquad (13)$$

It is important to note the difference between the angle of incidence θ_i shown in Fig. 4 and the angle of incidence θ_i' in the above equations. As shown in Fig. 5, the angle θ_i' is the "local" angle of incidence, i.e., the angle between the incident wave propagation vector $\boldsymbol{k}_1$ and the normal vector $\boldsymbol{n}'$ at a particular point on the surface. Therefore, θ_i' can vary over the surface, while θ_i is constant for a given incident wave. The term Y in the above equations is called the *normalized admittance* of the surface medium and is a function of the complex index of refraction η'. Hence, Y is also a function of the electrical properties of the medium. For a conductor, Y approaches infinity, while for a dielectric (nonconductor), Y is almost zero.

Let us now return to the problem of finding the scattered field E_2 by evaluating the Helmholtz integral given by (8). Assume that the surface under consideration is a rectangular patch of area A and dimensions $2X$ and $2Y$ in the x and y directions, respectively, i.e., $A = 4XY$. Further, assume that the observation point P is at a great distance from the surface compared to the physical dimensions of the surface patch and, as a result, the vector $\boldsymbol{k}_2$ is constant over the entire surface area. Then, the distance R' in Fig. 4 can be expressed as:

$$kR' = kR_o - \boldsymbol{k}_2 \cdot \boldsymbol{r}. \qquad (14)$$

By substituting (10), (11), and (14) in (8), the scattered field E_2 is found to be:

$$E_2 = \frac{E_{o1} ike^{ikR_o}}{4\pi R_o} \int_{-X}^{X} \int_{-Y}^{Y} (ah_x' + ch_y' - b) e^{i\mathbf{v}\cdot\mathbf{r}}\, dx\, dy \qquad (15)$$

where

$$\begin{aligned} v &= (\nu_x, \nu_y, \nu_z) = k(\sin\theta_i - \sin\theta_r \cos\phi_r)\boldsymbol{x} \\ &\quad + k(\sin\theta_r \sin\phi_r)\boldsymbol{y} - k(\cos\theta_i + \cos\theta_r)\boldsymbol{z} \\ a &= (1-F)\sin\theta_i + (1+F)\sin\theta_r\cos\phi_r \\ b &= (1+F)\cos\theta_r - (1-F)\cos\theta_i \\ c &= -(1+F)\sin\theta_r \sin\phi_r. \end{aligned} \tag{16}$$

The terms h'_x and h'_y denote the derivatives of the surface height $h(x, y)$ in the x and y directions, respectively. If the admittance of the surface is finite, the Fresnel coefficient F is a function of the local angle of incidence θ'_i [see (12) and (13)]. For a rough surface, θ'_i varies over the surface. As a result, the factors *a, b,* and *c* in (15) also vary over the surface. Therefore, for finite admittance, the integral becomes very cumbersome to evaluate and no solution to the scattering problem is known that is general and exact at the same time. This leads us to our next assumption: The surface medium is considered to be a perfect conductor, i.e., $Y \to \infty$. Then, from (12) and (13) we see that:

$$F_{\text{para}} = 1 \qquad \text{and} \qquad F_{\text{perp}} = -1 \tag{17}$$

and the terms *a*, *b*, and *c* in (15) are independent of x and y. Further, the incident wave is assumed to be of perpendicular polarization. Then $F = F_{\text{perp}} = -1$.

In order to evaluate the integral in (15), the height function $h(x, y)$ must be defined. The exact profile of the surface is of course not known to us. Even if the profile is determined by some method and used in (15), the result would only be valid for that particular profile. Our purpose is to develop a model that is applicable to a wide range of surface profiles. To this end, a parametrized stochastic model is used to represent the surface. Beckmann and Spizzichino have used the normal height distribution model described in Section II. The surface height is assumed to have a normal distribution function with mean value <*h*>= 0, standard deviation σ_h, and correlation distance T. The normal distribution $p_h(h)$ is given by (1) and the autocorrelation function $C(\tau)$ by (2). Since h and the scattered field E_2 are related by (15), the statistics of E_2 can be determined from the statistics of h. Beckmann and Spizzichino have presented detailed derivation for the mean field and mean power scattered by the surface in an arbitrary direction for any given angle of incidence. It turns out that the mean field <E_2> is non-zero in the specular direction ($\theta_r = \theta_i$) but tends rapidly toward zero as θ_r deviates from the specular direction. Since <E_2> is a complex quantity, its dependence on θ_i and θ_r is difficult to interpret. For instance, it does not follow from <E_2> = 0 that <$|E_2|$> = 0. Therefore, Beckmann and Spizzichino have only used <E_2> as a stepping stone to derive the *mean scattered power* <$E_2E_2^*$> = <$|E_2|^2$>. For a given incidence angle θ_i, the mean power scattered in the direction (θ_r, ϕ_r) by a rough surface whose height h is normally distributed with mean value <h> = 0, standard deviation σ_h, and correlation distance T, is:

$$<E_2E_2^*> = \frac{E_{o1}^2 A^2 \cos^2\theta_i}{\lambda^2 R_o^2} e^{-g} \cdot \left(\rho_o^2 + \frac{\pi T^2 D^2}{A} \sum_{m=1}^{m=\infty} \frac{g^m}{m!m} e^{-\nu_{xy}^2 T^2/4m} \right) \tag{18}$$

where

$$g = \left(2\pi \frac{\sigma_h}{\lambda} (\cos\theta_i + \cos\theta_r) \right)^2 \tag{19}$$

$$\rho_o = \text{sinc}(\nu_x X)\ \text{sinc}(\nu_y Y) \tag{20}$$

$$D = \left(\frac{1 + \cos\theta_i \cos\theta_r - \sin\theta_i \sin\theta_r \cos\phi_r}{\cos\theta_i(\cos\theta_i + \cos\theta_r)} \right) \tag{21}$$

$$\nu_{xy} = \sqrt{\nu_x^2 + \nu_y^2}. \tag{22}$$

The factor g in (18) is proportional to the square of the ratio[3] σ_h/λ. Therefore, g represents the roughness of the surface and the three cases $g \ll 1$, $g \approx 1$, and $g \gg 1$ correspond to smooth surfaces,[4] moderately rough surfaces, and very rough surfaces, respectively.

It may be pointed out that the model under consideration only describes the reflection mechanism that is referred to by the vision research community as "specular reflection." Specular reflection models used for vision have always had a single component [12], [25], [38]. Equation (18) indicates that the scattered energy is the sum of two terms. We refer to the first term, $e^{-g}\rho_o^2$, as the *specular spike* component. Equation (20) indicates that ρ_o is a very sharp function of θ_i and θ_r, and is nearly zero for all scattering directions except a very narrow range around the specular direction. We refer to the second term in (18) as the *specular lobe,*[5] i.e., the diffuse scattering of incident energy that results from the roughness of the surface. As we will see shortly, the specular lobe component is distributed around the specular direction. For a perfectly smooth surface, $g = 0$ and the specular lobe vanishes, while the specular spike is strong. As the roughness measure g increases, the spike component shrinks rapidly, and the lobe component increases in magnitude.

The exponential series given by the summation in the lobe component can be approximated for smooth ($g \ll 1$) and very rough ($g \gg 1$) surfaces. The approximations result in simpler expressions for the scattered power for these two extreme surface conditions:

$$<E_2E_2^*>_{\text{smooth}} = \frac{E_{o1}^2 A^2 \cos^2\theta_i}{\lambda^2 R_o^2} \cdot e^{-g} \left(\rho_o^2 + \frac{\pi T^2 D^2 g}{A} e^{-\nu_{xy}^2 T^2/4} \right) \qquad (g \ll 1) \tag{23}$$

[3] In physical optics the ratio σ_h/λ is referred to as the *optical roughness* of the surface.

[4] We define a smooth surface as one that is either perfectly smooth or "slightly" rough.

[5] Beckmann and Spizzichino have referred to this component as the diffuse component. The term "diffuse" has historically been used by the vision community to describe the reflection component that results from other mechanisms such as internal scattering. To avoid confusion we will refer to the diffuse component of specular reflection as the specular lobe.

$$<E_2E_2^*>_{\text{rough}} = \frac{E_{o1}^2 A\cos^2\theta_i \pi T^2 D^2}{\lambda^2 R_o^2 \nu_z^2 \sigma_h^2} \exp\left(\frac{-\nu_{xy}^2 T^2}{4\nu_z^2\sigma_h^2}\right) \quad (g \gg 1). \quad (24)$$

The above equations for scattered power represent the Beckmann–Spizzichino reflectance model. It is important to understand the conditions that determine the validity of the model. We therefore summarize the assumptions made during the derivation of the model and discuss the restrictions imposed by these assumptions.

2) Assumptions and Related Comments:

- The surface height is assumed to be normally distributed. However, Beckmann and Spizzichino have derived reflectance models for surfaces with other height distributions, including surfaces with periodic profiles.
- The radius of curvature of surface irregularities is large compared to the wavelength of incident light (Kirchoff's assumption). This assumption is necessary to approximate the electromagnetic field at the surface and its normal derivative. The approximation breaks down when the surface irregularities include sharp edges or sharp points.
- The surface is assumed to be a perfect conductor. This assumption forces the quantities a, b, and c in (15) to be constants, thus making it possible to evaluate the Helmholtz integral. It is possible to approximate the scattered field and power for surfaces of finite conductivity by averaging the Fresnel coefficient F over the entire surface area and using the resultant value $<F>$ as a constant in the Helmholtz integral. This way the mean field and mean power scattered by surfaces of finite conductivity are determined [1] as:

$$<E_2>_f = <F><E_2>_\infty \quad (25)$$

$$<E_2E_2^*>_f = <FF^*><E_2E_2^*>_\infty \quad (26)$$

  where the indices f and ∞ denote finite and infinite conductivity, respectively.
- The *masking* and *shadowing* of surface points by adjacent surface points is ignored. Adjacent points may obstruct either the wave incident at a given point or the waves scattered from it. Clearly, these effects are related to the angles of incidence and reflection. It is possible to compensate for the shadowing and masking effects by replacing the height function $h(x,y)$ by $S(x,y)h(x,y)$. $S(x,y)$ is a shadowing function [32] that tends toward unity for surface points that are illuminated and zero for those that are not.
- It is assumed that the incident wave is reflected only once and does not bounce between surface points before it is scattered in the direction of the observation point P. Without this assumption it would be very difficult to compute the scattered field; no closed-form solution that takes *multiple scatterings* into account is known at the present time.
- The incident wave is assumed to be perpendicularly polarized. The mean field and power can also be determined for parallel polarization. Beckmann and Spizzichino have also discussed possible approaches for solving the scattering problem when the polarization vector e_1 of the incident wave is neither parallel nor perpendicular to the plane of incidence.
- The incident wave is assumed to be a plane wave. This assumption is reasonable when the source is at a great distance from the surface relative to the physical dimensions of the surface. If the source is close to the surface, the incident waves must be considered to be spherical.

3) Surface Radiance from Scattered Power: The Beckmann–Spizzichino reflectance model predicts the mean field and mean power scattered by a surface. In machine vision, radiometric terms are generally used to describe the brightness and reflectance of a surface. Some of these terms are defined in Appendix B. The amount of light falling on a surface is called the *irradiance*. It is the power per unit area (watts per square meter) incident on the surface. The amount of light radiated from the surface is called the *radiance*. It is the power per unit area per unit solid angle (watts per square meter per steradian) emitted from the surface. Horn has shown that image irradiance is proportional to scene radiance [14]. Therefore, it is convenient to express the brightness of a surface in terms of its radiance. In Appendix C, we have derived surface radiance from the scattered power given by (18). The final result is:

$$L_r = \sqrt{\frac{\mu}{\varepsilon}} \frac{E_{o1}^2 \cos^2\theta_i}{2\lambda^2} e^{-g} \left(\left(\frac{z}{f}\right)^2 \frac{dA_{im}\cos\gamma}{\cos^2\theta_r} \rho_o^2 + \frac{\pi T^2 D^2}{\cos\theta_r} \sum_{m=1}^{m=\infty} \frac{g^m}{m!\,m} e^{-\nu_{xy}{}^2 T^2/4m} \right). \quad (27)$$

The radiance expressions for the special cases of smooth and rough surfaces are also derived from (23) and (24), respectively:

$$L_{r\text{smooth}} = \sqrt{\frac{\mu}{\varepsilon}} \frac{E_{o1}{}^2 \cos^2\theta_i}{2\lambda^2} e^{-g} \cdot \left(\left(\frac{z}{f}\right)^2 \frac{dA_{im}\cos\gamma}{\cos^2\theta_r} \rho_o^2 + \frac{\pi T^2 D^2 g}{\cos\theta_r} e^{-\nu_{xy}^2 T^2/4} \right) \quad (g \ll 1) \quad (28)$$

$$L_{r\text{rough}} = \sqrt{\frac{\mu}{\varepsilon}} \frac{E_{o1}{}^2 \cos^2\theta_i \pi T^2 D^2}{2\lambda^2 \cos\theta_r \nu_z^2 \sigma_h^2} \cdot \exp\left(\frac{-\nu_{xy}^2 T^2}{4\nu_z^2\sigma_h^2}\right) \quad (g \gg 1). \quad (29)$$

We conclude this section with the following observations:

- The Beckmann–Spizzichino model has two components: the specular spike and lobe components.
- The model can describe reflection from smooth and rough surfaces.
- The general expression for surface radiance is a fairly complicated function of the angles of incidence and reflection, and the surface roughness parameters.

In the following section, we describe a reflectance model based on geometrical optics. Subsequently, we compare the two models, highlighting the main differences and similarities.

B. Geometrical Optics Model

Geometrical optics is applicable in situations where the electromagnetic character of light can be ignored. In the context of reflection, this is possible when the wavelength of incident light is much smaller than the dimensions of the surface irregularities. The incident light may be thought of as a collection of rays where each ray travels in a straight line in a homogeneous medium. Further, each ray may be assumed to be specularly reflected by the surface, i.e., the angle of reflection equals the angle of incidence. Under these assumptions, a reflectance model may be derived using purely geometrical analysis. It is important to note that geometrical optics is a limiting case of physical optics. In general, it is not valid when the surface roughness is comparable to the wavelength of incident light.

In this section, we present the Torrance–Sparrow reflectance model. This model uses geometrical optics to describe the specular reflection mechanism. Torrance and Sparrow have appended the Lambertian model to their reflectance model to account for the internal scattering mechanism. We briefly describe the Lambertian model[6] and then proceed to describe the Torrance–Sparrow model. Once again, our intention is to highlight the main steps in the derivation of the model and clearly state the assumptions made during the derivation. In the next section, reflectance plots predicted using the Torrance–Sparrow model are presented. On the basis of these reflectance plots, the Torrance–Sparrow model is compared with the Beckmann–Spizzichino physical optics model.

1) Lambertian Model: Lambert [19] was the first to investigate the mechanism underlying diffuse reflection. Surfaces that satisfy Lambert's law appear equally bright from all directions. In other words, the radiance of a Lambertian surface is independent of the viewing direction. The main mechanism that produces Lambertian reflection is called *internal scattering*. Incident light rays penetrate the surface and encounter microscopic inhomogeneities in the surface medium (Fig. 6). The rays are repeatedly reflected and refracted at boundaries between regions of differing refractive indices. Some of the scattered rays find their way to the surface with a variety of directions, resulting in diffuse reflection. When the internal scattering mechanism produces constant surface radiance in all directions, we have Lambertian reflection.

The radiance of a Lambertian surface is proportional to its irradiance. Consider an infinitesimal surface area dA_s illuminated by an infinitesimal source area dA_i, as shown in Fig. 7. The flux incident on dA_s is determined from the source radiance L_i as:

$$d\Phi_i = L_i d\omega_s \, dA_i. \tag{30}$$

[6]Lambertian reflection is normally categorized as "body" reflection rather than surface reflection. The model is discussed here only because it is used later to represent one of the primary reflection components.

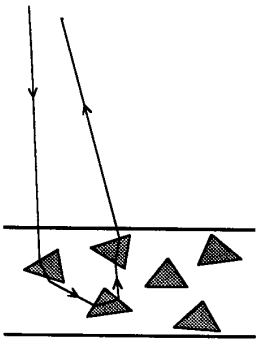

Fig. 6. Diffuse reflection resulting from the internal scattering mechanism.

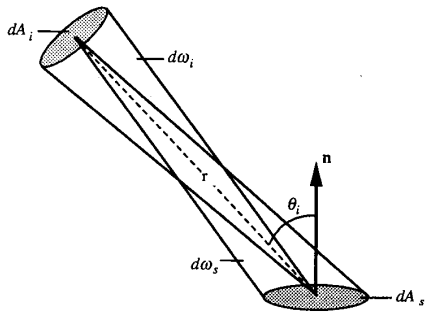

Fig. 7. Solid angles subtended by the surface element and the source.

From the solid angles subtended by the surface and source areas, we obtain:

$$dA_i = d\omega_i r^2 \tag{31}$$

$$d\omega_s = \frac{dA_s \cos\theta_i}{r^2}. \tag{32}$$

Substituting (31) and (32) into (30), we obtain:

$$d\Phi_i = L_i \, d\omega_i dA_s \cos\theta_i. \tag{33}$$

Surface irradiance is determined as:

$$I_s = \frac{d\Phi_i}{dA_s}. \tag{34}$$

As stated earlier, the radiance L_r of a Lambertian surface is proportional to its irradiance I_s. Note that I_s is zero when the angle of incidence exceeds $\pi/2$. Hence, surface radiance may be written as:

$$L_r = \kappa_{\text{diff}} \max[0, (L_i d\omega_i \cos\theta_i)] \tag{35}$$

where κ_{diff} determines the fraction of the incident energy that is diffusely reflected by the surface. The above expression for radiance represents the Lambertian reflectance model.

1) Torrance–Sparrow Model: The Torrance–Sparrow model describes single reflection of incident light rays by rough surfaces [38]. Based on geometrical optics, the model is valid only when the wavelength of light is much smaller than the roughness of the surface, i.e., $\lambda \ll \sigma_h$. Torrance and Sparrow have used the slope distribution model (Section II) to represent

the profile of the surface. The surface is assumed to be a collection of planar micro-facets. The micro-facets are much larger in dimensions than the wavelength of incident light. The facets are also perfectly smooth, i.e., they are specular (mirror-like) in reflectance. The orientation of each facet deviates from the mean orientation of the surface by an angle α; α is referred to as the facet slope and is a random variable. Torrance and Sparrow have assumed α to be normally distributed. The surface is also assumed to be isotropic. Hence, the distribution function is rotationally symmetric and can be represented by a one-dimensional normal distribution function:

$$\rho_\alpha(\alpha) = ce^{-\frac{\alpha^2}{2\sigma_\alpha^2}} \tag{36}$$

where c is a constant, and the facet slope α has mean value $<\alpha> = 0$ and standard deviation σ_α. As we have stated earlier, for this surface model, roughness is represented by the parameter σ_α. Noting that α can only vary between 0 and $\pi/2$, the constant c is determined as:

$$c = 1 \Big/ \int_0^{\pi/2} e^{-\frac{\alpha^2}{2\sigma_\alpha^2}}\, d\alpha. \tag{37}$$

Consider the geometry shown in Fig. 8. The surface area dA_s is located at the origin of the coordinate frame, and its normal vector points in the direction of the z axis. The surface is illuminated by a beam of light that lies in the $x - z$ plane and is incident on the surface at an angle θ_i. We are interested in determining the radiance of the surface in the direction (θ_r, ϕ_r). Only those planar micro-facets whose normal vectors lie within the solid angle $d\omega'$ are capable of specularly reflecting light into the infinitesimal solid angle $d\omega_r$. Using spherical trigonometry, the local angle of incidence θ_i' and slope α of the reflecting facets can be determined from the angles θ_i, θ_r, and ϕ_r:

$$\theta' = \frac{1}{2}\cos^{-1}(\cos\theta_r\cos\theta_i - \sin\theta_r\sin\theta_i\cos\phi_r) \tag{38}$$

$$\alpha = \cos^{-1}\left(\cos\theta_i\cos\theta_i' + \sin\theta_i\sin\theta_i'\cos \cdot(\sin^{-1}(\sin\phi_r\sin\theta_r/\sin 2\theta_i'))\right). \tag{39}$$

The number of facets per unit surface area whose normal vectors lie within the solid angle $d\omega'$ is equal to $\rho_\alpha(\alpha)d\omega'$. Let a_f be the area of each facet. Then, the area of points on dA_s that reflect light from the direction θ_i into the solid angle $d\omega_r$ is equal to $a_f\rho_\alpha(\alpha)d\omega' dA_s$. All the reflecting facets are assumed to have the same local angle of incidence θ_i'. From (33), the flux incident on the set of reflecting facets is determined as:

$$d^2\Phi_i = L_i\, d\omega_i[a_f\rho_\alpha(\alpha)\, d\omega' dA_s]\cos\theta_i'. \tag{40}$$

The fraction of incident light that is reflected by a facet is determined by the Fresnel reflection coefficient. As described in the previous section, the Fresnel coefficients $F_{\text{para}}(\theta_i', \eta')$ and $F_{\text{perp}}(\theta_i', \eta')$ represent the electromagnetic field reflected in the specular direction by a planar surface when the incident wave is of parallel and perpendicular polarization,

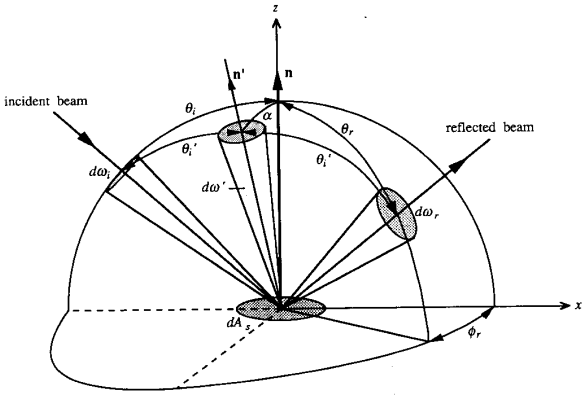

Fig. 8. Coordinate system used to derive the Torrance–Sparrow model.

respectively. In this section, however, we are interested in the reflected flux, i.e., the energy flowing through unit area. The Fresnel coefficients for energy reflectance can be determined from those for field reflectance as:

$$F'_{\text{para}}(\theta_i', \eta') = |F_{\text{para}}(\theta_i', \eta')|^2$$
$$F'_{\text{perp}}(\theta_i', \eta') = |F_{\text{perp}}(\theta_i', \eta')|^2. \tag{41}$$

Assume that the polarization vector e_1 of the incident light wave lies outside the plane of incidence. Let h and v represent the magnitudes of the resolved components of e_1 in the parallel and perpendicular polarization planes, respectively. The Fresnel coefficient $F'(\theta_i', \eta')$ can be expressed as a linear combination of the Fresnel coefficients for parallel and perpendicular incident waves [30]:

$$F'(\theta_i', \eta') = hF'\text{para}(\theta_i', \eta') + vF'_{\text{perp}}(\theta_i', \eta') \tag{42}$$

where

$$h, v \geq 0 \quad \text{and} \quad h + v = 1. \tag{43}$$

Torrance and Sparrow have also considered the masking and shadowing of micro-facets by adjacent facets. Adjacent facets may obstruct flux incident upon a given facet or the flux reflected by it. In order to compensate for these effects, the *geometrical attenuation factor*[7] $G(\theta_i, \theta_r, \phi_r)$ is introduced. The obstruction of incident or reflected light depends on the angle of incidence and the angles of reflection. Each facet is assumed to be one side of a V-groove cavity, and light rays are assumed to be reflected only once. A detailed derivation of $G(\theta_i, \theta_r, \phi_r)$ is given in [38]. The result is:

$$G(\theta_i, \theta_r, \phi_r) = \min\left(1, \frac{2\cos\alpha\cos\theta_r}{\cos\theta_i'}, \frac{2\cos\alpha\cos\theta_i}{\cos\theta_i'}\right). \tag{44}$$

Taking the Fresnel reflection coefficient and the geometrical attentuation factor into account, the flux $d^2\Phi_r$ reflected into

[7]This factor plays the role of the shadowing function $S(x, y)$ mentioned in Section III-A-2.

the solid angle $d\omega_r$ may be determined from the flux $d^2\Phi_i$ incident on the reflecting facets as:

$$d^2\Phi_r = F'(\theta_i', \eta')G(\theta_i, \theta_r, \phi_r)d^2\Phi_i. \quad (45)$$

The radiance of the surface element dA_s in the direction (θ_r, ϕ_r) is defined as:

$$L_r = \frac{d^2\Phi_r}{d\omega_r dA_s \cos\theta_r}. \quad (46)$$

Substituting (40) and (45), into (46), we obtain:

$$L_r = \frac{F'(\theta_i', \eta')G(\theta_i, \theta_r, \phi_r)L_i\, d\omega_i a_f \rho_\alpha(\alpha) d\omega' dA_s \cos\theta_i'}{d\omega_r\, dA_s \cos\theta_r}. \quad (47)$$

Earlier, we stated that only facets with normals that lie within the solid angle $d\omega'$ are capable of reflecting light into the solid angle $d\omega_r$. $d\omega'$ and $d\omega_r$ are related to one another as:

$$d\omega' = \frac{d\omega_r}{4\cos\theta_i'}. \quad (48)$$

Torrance and Sparrow have only used the above relation and have not derived it. However, this relation is a very important one as it provides insight into the reasons for which the model is not applicable to perfectly smooth surfaces. For the interested reader, a derivation of the above relation is provided in Appendix D.

Substituting (36) and (48) into (47), we obtain:

$$L_r = \kappa_{\text{spec}} \frac{L_i d\omega_i}{\cos\theta_r} e^{-\frac{\alpha^2}{2\sigma_\alpha{}^2}} \quad (49)$$

where

$$\kappa_{\text{spec}} = \frac{c a_f F'(\theta_i', \eta')G(\theta_i, \theta_r, \phi_r)}{4}. \quad (50)$$

Note the similarity between the above equation and the expression for the specular lobe component of the Beckmann–Spizzichino model [see (29)]. It is clear that the Torrance–Sparrow model describes only the lobe component of specular reflection; there is no term in the above equation that represents the spike component. Surface radiance is determined only by the roughness parameter σ_α, and unlike the Beckmann–Spizzichino model, there is no dependence on the wavelength λ of incident light. However, from the physical optics model we have seen that the spike component is significant only when $\sigma_h/\lambda < 1.5$. Torrance and Sparrow have clearly stated that their model is, in general, valid only when $\sigma_h/\lambda \gg 1.0$. Therefore, this model must **not** be used to predict or interpret reflections from very smooth surfaces, i.e., when $\sigma_h/\lambda \ll 1.0$. To make their model more general, Torrance and Sparrow have appended the Lambertian model to their model to account for diffuse reflections that may result from internal scattering. Thus, for an angle of incidence θ_i, the radiance in the direction (θ_r, ϕ_r) of a rough surface whose facet slopes are normally distributed with standard deviation σ_α is:

$$L_r = \kappa_{\text{diff}} \max[0, (L_i\, d\omega_i \cos\theta_i)] + \kappa_{\text{spec}} \frac{L_i\, d\omega_i}{\cos\theta_r} e^{-\frac{\alpha^2}{2\sigma_\alpha{}^2}} \quad (51)$$

where κ_{diff} and κ_{spec} represent the fractions of incident energy that are reflected by the diffuse and specular mechanisms, respectively. Once again, we summarize the assumptions made during the derivation of this model and discuss the restrictions imposed by these assumptions.

3) Assumptions and Related Comments:

- The surface is modeled as a collection of planar microfacets, and the facet slopes are assumed to be normally distributed. Note that the slope distribution function $\rho_\alpha(\alpha)$ appears explicitly in the final expression for surface radiance, (51). Therefore, any distribution function can be used in place of the normal distribution without having to re-derive the reflectance model.
- The size of the planar facets is much greater than the wavelength of incident light, i.e., $\sigma_h \gg \lambda$. Therefore, it can be assumed that the incident light rays are reflected by each facet in its specular direction only. Furthermore, $\sigma_h \gg \lambda$ implies that the spike component of reflection is zero and that the model represents only the lobe component of reflection.
- The model takes the Fresnel reflection coefficient F' into account. Therefore, no assumptions need to be made regarding the polarization of incident light and the conductivity of the surface medium. As a result, the model is capable of predicting reflections from both conductors and dielectrics.
- Each facet is one side of a symmetric V-groove cavity. With this assumption, the shadowing and masking effects are accounted for by using the geometrical attenuation factor G.
- The source is assumed to be at a great distance from the surface so that all light rays incident on the surface area dA_s are nearly parallel to one another. This assumption simplifies the relationship between the solid angles $d\omega'$ and $d\omega_r$, [see (48)].
- The final model includes the Lambertian model to account for diffuse reflection resulting from internal scattering.

IV. A Unified Perspective

We have described reflectance models based on both physical optics and geometrical optics and stated the assumptions under which they are valid. Physical optics models are derived using electromagnetic wave theory. They are more general than models based on geometrical optics in that they can describe reflection from smooth and rough surfaces. However, physical models are often inappropriate for use in machine vision as they have functional forms that are difficult to manipulate. Geometrical models, on the other hand, are derived by analyzing the surface and illumination geometry and have simpler functional forms. These models, however, are approximations to physical models and in general are not capable of describing reflection from smooth surfaces.

In this section, we compare the Beckmann–Spizzichino (physical optics) and Torrance–Sparrow (geometrical optics) reflectance models on the basis of reflectance plots predicted by them. By studying the reflectance plots, we identify the primary components of reflection. We then propose a unified reflectance framework for machine vision that has the functional simplicity of a geometrical reflectance model as well as the completeness of a physical reflectance model. Two representations for the reflectance framework are presented that are important from the perspective of vision. In the first case, the primary components are plotted as a function of the angle of reflection (sensor direction) for a given angle of incidence (source direction). In the second case, the components are plotted as a function of the angle of incidence for a given angle of reflection. We conclude this section with a brief discussion on how the unified reflectance framework may be used, and we show that several shape recovery methods used in vision are based on reflectance models that fall within the proposed framework.

A. Physical Optics Model versus Geometrical Optics Model

The Beckmann–Spizzichino and Torrance–Sparrow models are compared by studying reflectance plots predicted by the two models for different surface roughness values. Traditionally, the bidirectional reflectance distribution function (BRDF) has been used to represent surface reflectance. The BRDF is the radiance of the surface normalized by its irradiance. In machine vision, we are interested in interpreting image irradiance (intensity) values. Horn [14] showed that image irradiance is proportional to surface radiance. For this reason, and others that will be given shortly, we use radiance as measure of the reflectance of the surface. Radiance is plotted as a function of the viewing angles (θ_r, ϕ_r) and the incidence angle θ_i. We refer to these plots as *radiance diagrams.* For each of the two models, radiance diagrams are generated for different values of the surface roughness parameters. The radiance diagrams are then used to analyze and compare the behavior of the two models.

1) Radiance Diagrams for Beckmann–Spizzichino Model: The radiance diagrams presented here are generated using following radiance expressions for the Beckmann–Spizzichino model.

$$L_r = \sqrt{\frac{\mu}{\varepsilon}}\frac{{E_{o1}}^2\cos^2\theta_i}{2\lambda^2}e^{-g}\left(\left(\frac{z}{f}\right)^2\frac{dA_{im}\cos\gamma}{\cos^2\theta_r}{\rho_0}^2 + \frac{\pi T^2 D^2}{\cos\theta_r}\sum_{m=1}^{m=\infty}\frac{g^m}{m!\,m}e^{-{v_{xy}}^2T^2/4m}\right) \quad (52)$$

$$L_{r\text{rough}} = \sqrt{\frac{\mu}{\varepsilon}}\frac{{E_{o1}}^2\cos^2\theta_i\pi T^2D^2}{2\lambda^2\cos\theta_r{\nu_z}^2{\sigma_h}^2}\exp\left(\frac{-{\nu_{xy}}^2T^2}{4{\nu_z}^2{\sigma_h}^2}\right) \quad (g \gg 1) \quad (53)$$

where L_r and $L_{r\text{rough}}$ are the general expression for radiance and its approximation for rough surfaces, respectively. λ is the wavelength of incident light, σ_h is the standard deviation of the surface height, T is the correlation distance for the surface variations, θ_i is the angle of incidence, and θ_r is the angle of reflection. For simplicity it is assumed that the observation point lies in the plane of incidence, i.e., $\phi_r = 0$. In each diagram, radiance is plotted as a function of θ_r for fixed values of θ_i.

The reflectance characteristics of the surface depend on its roughness with respect to the wavelength of incident light and the frequency of its spatial variation. The roughness of the surface is determined by the factor g which in turn is a function of the optical roughness σ_h/λ [see (19)]. The frequency of spatial variation is determined by the ratio σ_h/T (Section II). We are interested in studying how the radiance diagrams are affected by the two ratios σ_h/λ and σ_h/T. The two ratios are varied by keeping σ_h constant and varying λ and T, respectively. Fig. 9 shows radiance diagrams for different values of σ_h/λ. All the diagrams are generated using the general radiance expression given by (52). The specular lobe component of radiance was computed by summing the first 100 terms of the exponential series.

In Fig. 9(a), $\sigma_h/\lambda = 0.002$, i.e., $g \approx 0$. From (52) we see that, when $g \approx 0$, the lobe component is near zero and the spike component is dominant. The surface behaves in a mirror-like manner and reflects light only in the specular direction $\theta_r = \theta_i$. Also note that the radiance in the specular direction is constant for different values of θ_i. This is consistent with our real-world experience; when we look at a perfect mirror from the specular angle, we see a virtual image of the source. Further, the image appears the same irrespective of the angle of incidence. Through numerous simulations, we have found that this mirror-like behavior is observed when $\sigma_h/\lambda < 0.025$. In Fig. 9a, the spike component looks like a delta function. However, the spike component is really the square of a *sinc* function [see (20)]. This is seen in Fig. 9(b), where one of the radiance plots in Fig. 9(a) is rescaled and plotted.

As σ_h/λ is increased above 0.025 [Fig. 9(c) and (d)], the spike component decreases rapidly in magnitude. However, the spike component is still strong for large values of θ_r and θ_i.This is because g is a function not only of σ_h/λ but also of $(\cos\theta_i + \cos\theta_r)$. Hence, for large values of θ_i and θ_r, g approaches zero, the spike component increases, and the surface tends to behave like a mirror. However, when σ_h/λ is increased further [(Fig. 9(e) and (f)], the spike component fades away, and the lobe component begins to dominate the radiance value. We have observed that, when $\sigma_h/\lambda > 1.5$, the spike component disappears for incidence angles that are not close to the grazing angle, and the radiance value is determined solely by the lobe component.

Fig. 10 shows that the shape and magnitude of the lobe component are greatly affected by the ratio σ_h/T. In Fig. 10(a), radiance diagrams generated by using the general expression (52) and the approximate radiance expression for rough surfaces (53) are compared. $L_{r\text{rough}}$ seems to provide a good approximation to the lobe component of L_r. Hence, $L_{r\text{rough}}$ may be used instead of L_r when the spike component is negligible. In Fig. 10(b), the lobe component is sharp and concentrated around the specular direction. We have observed that when $\sigma_h/T < 0.02$, the shape of the lobe

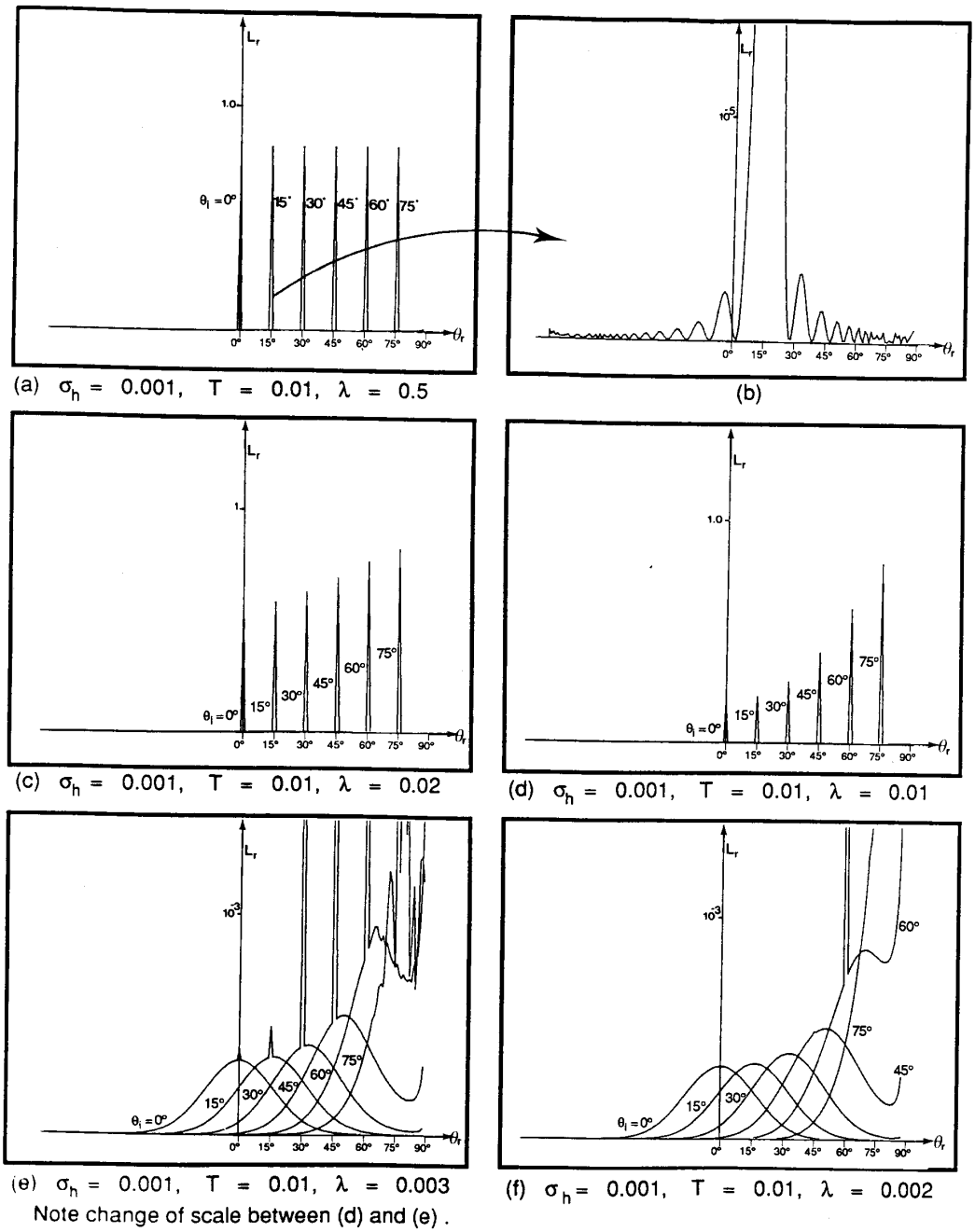

Fig. 9. Radiance diagrams for the Beckmann–Spizzichino model: σ_h/λ equals (a) 0.002; (c) 0.05; (d) 0.1; (e) 0.33; (f) 0.5.

component resembles that of the spike component. However, the magnitude of the lobe peak increases with the incidence angle θ_i. This effect results from the term $1/\cos\theta_r$ in (53). As the ratio σ_h/T increases, the lobe gets wider and the lobe peak decreases in magnitude. In fact, for $\sigma_h/T < 0.05$, the lobes may be approximated by Gaussian functions with mean values corresponding to the specular direction ($\theta_i = \theta_r$). For larger values of σ_h/T, however, the lobe begins to peak at viewing angles greater than the specular angle; these are called *off-specular peaks*. Also note that as θ_r approaches 90 degrees, the radiance values approach infinity. By using a shadowing function, this effect can be avoided while preserving the shape of radiance curve for lower values of θ_r.

2) Radiance Diagrams for Torrance–Sparrow Model: Torrance and Sparrow have evaluated the performance of their

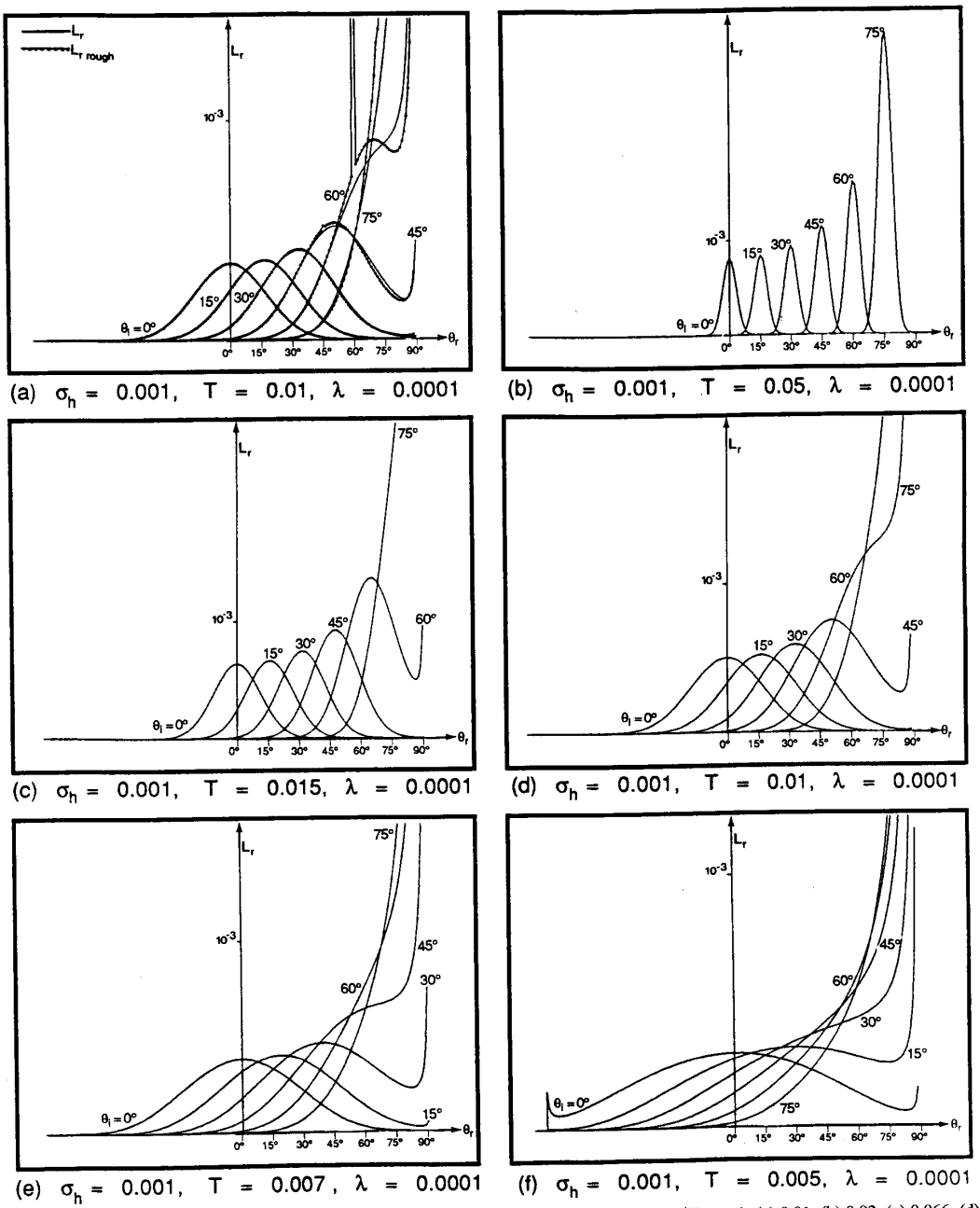

Fig. 10. Radiance diagrams for the specular lobe component of the Beckmann–Spizzichino model: σ_h/T equals (a) 0.01; (b) 0.02; (c) 0.066; (d) 0.1; (e) 0.2.

model by plotting the ratio of the BRDF in viewing direction to the BRDF in the specular direction. The normalized BRDF distributions predicted by the model for a dielectric (MgO) and a conductor (Al) were found to fit experimental data very well [38]. Here, we once again plot radiance diagrams to study the behavior of the model. Our main objective is to compare the Torrance–Sparrow model with the Beckmann–Spizzichino model. Hence, the Lambertian component of the Torrance–Sparrow is ignored. Radiance is computed using the expression:

$$L_r = \kappa_{\text{spec}} \frac{L_i \, d\omega_i}{\cos\theta_r} \, e^{-\frac{\alpha^2}{2\sigma_\alpha^2}} \tag{54}$$

where

$$\kappa_{\text{spec}} = \frac{c a_f F'(\theta_i', \eta') G(\theta_i, \theta_r, \phi_r)}{4}. \tag{55}$$

σ_α is the standard deviation of the slope (α) of individual micro-facets, θ_i is the angle of reflection, θ_r is the angle of re-

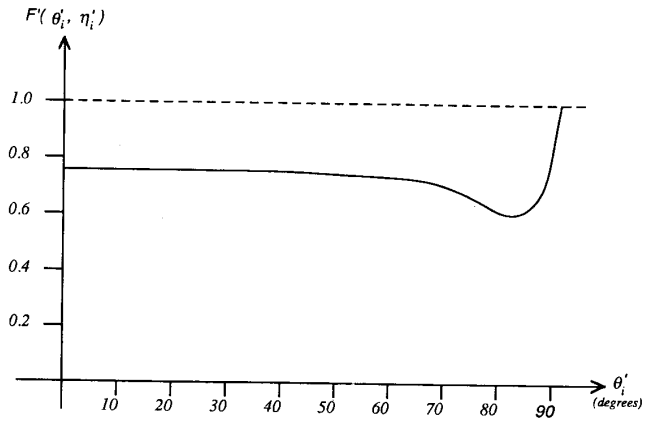

Fig. 11. Typical plot of the Fresnel reflection coefficient for a metal.

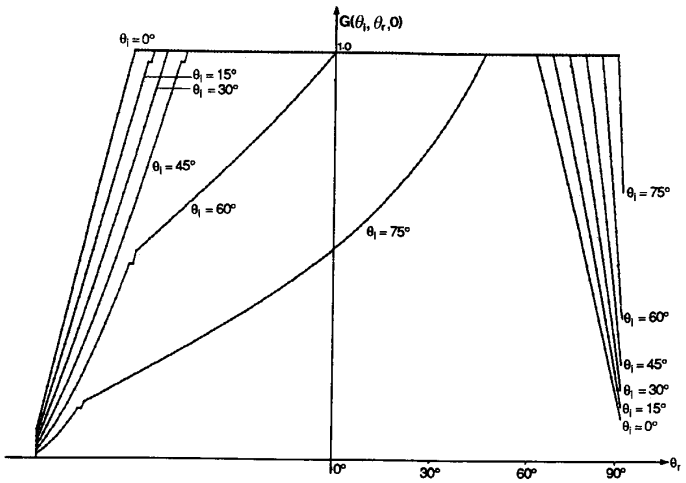

Fig. 12. Geometrical attentuation factor plotted as a function of the viewing angle for different values of the incidence angle.

flection, $F'(\theta', \eta')$ is the Fresnel coefficient, and $G(\theta_i, \theta_r, \phi_r)$ is the geometric attentuation factor.

Two assumptions are made with respect to the Fresnel coefficient $F'(\theta_i', \eta')$ and the geometrical attentuation factor $G(\theta_i, \theta_r, \phi_r)$ in (55). A typical plot of $F'(\theta_i', \eta')$ as a function of θ_i' for a metal is shown in Fig. 11. For both metals and non-metals, it is observed [26] that F' is nearly constant until the local angle of incidence θ_i' approaches around 75 degrees. Therefore, we assume that F' is constant with respect to θ_i and θ_r. Fig. 12 shows $G(\theta_i, \theta_r, \phi_r)$ plotted as a function of θ_r, for different values of θ_i. Note that for angles of incidence away from the grazing angle, G equals unity over a large range of θ_r values. In the following radiance diagrams, we will see that it is within these ranges of θ_r that surface radiance attains maximum values. Therefore, we assume that $G = 1$ for all values of θ_i and θ_r. With the above two assumptions, κ_{spec} is constant for all values of θ_i and θ_r.

Fig. 13 shows radiance diagrams for different values of the roughness parameter σ_α. Very small values of σ_α correspond to smooth surfaces. For smooth surfaces, the spike component is much stronger than the lobe component. However, the Torrance–Sparrow model represents only the specular lobe and not the specular spike. The specular lobes in Fig. 13(a) are sharp and similar in appearance to the specular spikes predicted by the Beckmann–Spizzichino model [Fig. 9(a)]. However, the peak values of the lobes in Fig. 13(a) increase with the angle of incidence while the peak values of the spikes predicted by the Beckmann–Spizzichino model [Fig. 9(a)] are constant. If the normalized BRDF is plotted rather than the radiance, the lobe peaks would also have constant values for all angles of incidence. As a result, the above mentioned difference in the spike and lobe component would not be apparent. It is for this reason that we have chosen to plot radiance rather than normalized BRDF.

In all the radiance diagrams in Fig. 13, the peak value of the specular lobe increases in magnitude with the angle of incidence θ_i. As with the Beckmann–Spizzichino model, this effect results from the term $1/\cos\theta_r$ [see (54)]. It is also clear

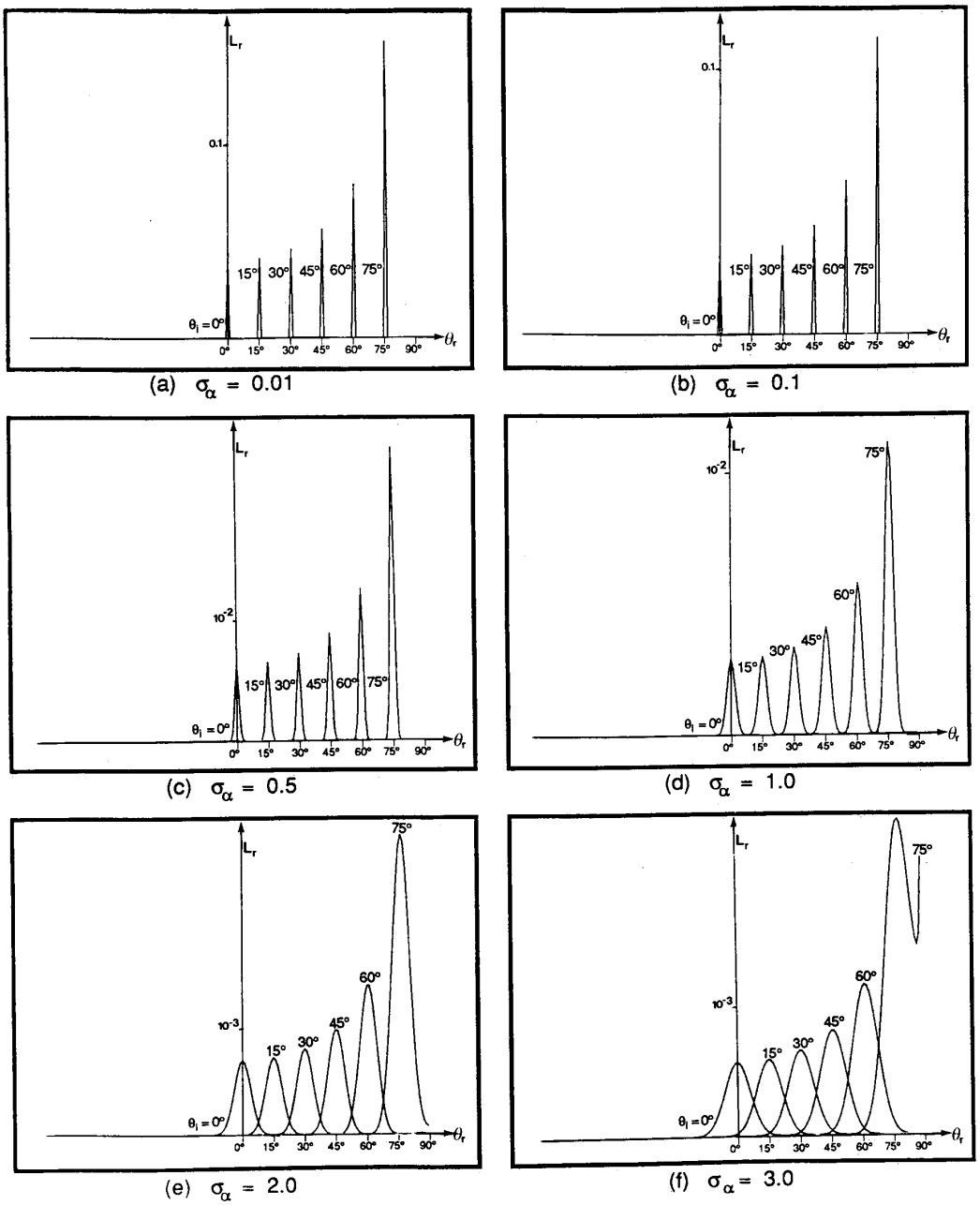

Fig. 13. Radiance diagrams for the Torrance-Sparrow model: σ_α equals (a) 0.01; (b) 0.1; (c) 0.5; (d) 1.0: (e) 2.0: (f) 3.0.

that the width of the lobe increases with the roughness parameter σ_α. In fact, for relatively small values of σ_α, the lobe may be approximated by a Gaussian function that is symmetric with respect to the specular direction. However, for higher values of σ_α (Fig. 14), the lobe peak occurs at reflection angles greater than the specular angle. As with the Beckmann–Spizzichino model, these off-specular peaks result from the term $1/\cos\theta_r$ in (54). For large values of θ_i and near-grazing values of θ_r, the radiance values approach infinity. However, from Fig. 12 we see that the geometrical attentuation factor G approaches zero as θ_r approaches the grazing angle. Torrance and Sparrow have shown that G approaches zero at a faster rate than the rate at which the plotted radiance approaches infinity. Hence, in practice, surface radiance approaches zero as θ_r approaches 90 degrees.

In Fig. 14(d), radiance diagrams predicted by the Torrance–Sparrow model and the Beckmann–Spizzichino model (approximation for rough surfaces) are shown together. Though

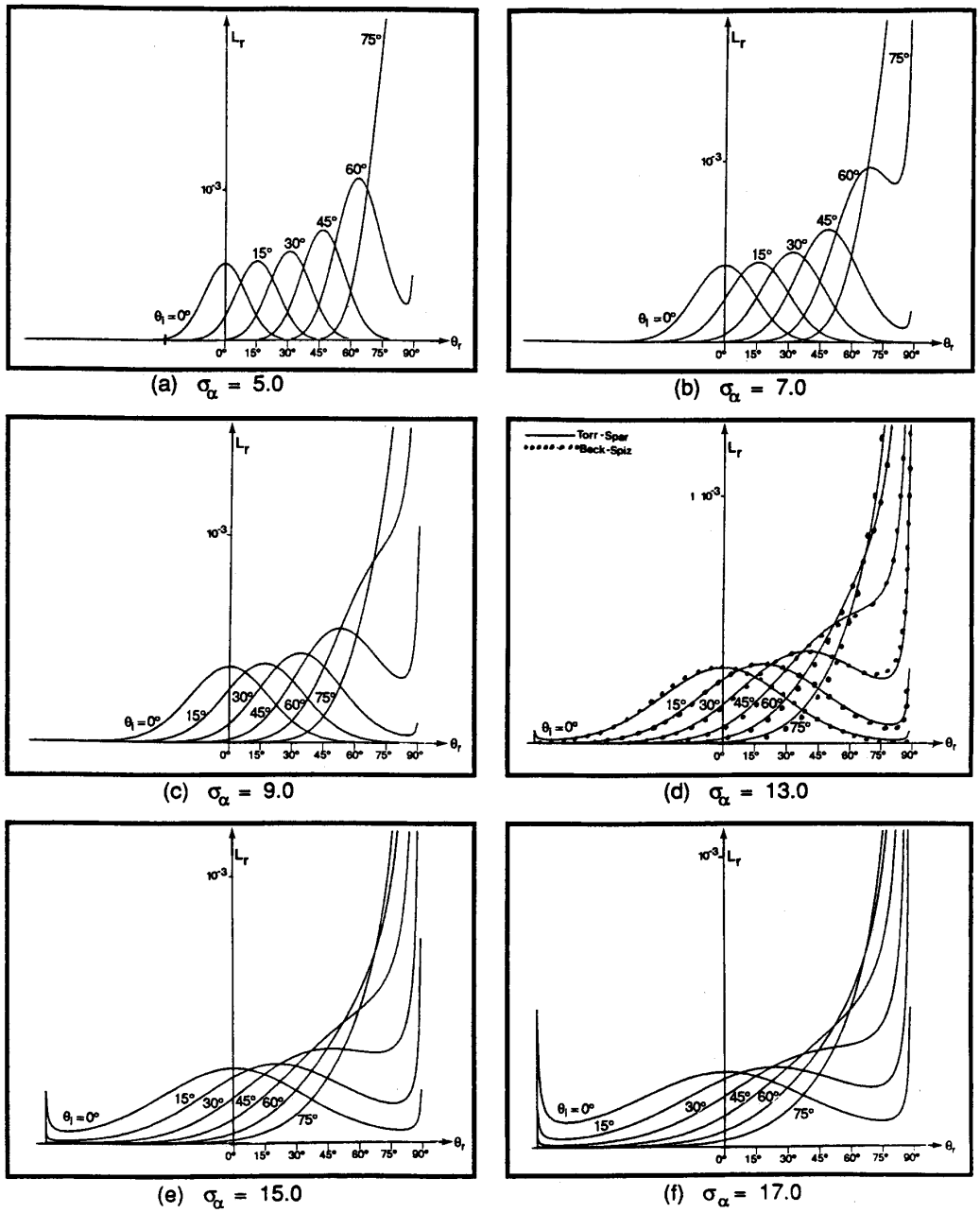

Fig. 14. Radiance diagrams for the Torrance–Sparrow model: σ_α equals (a) 5.0; (b) 7.0; (c) 9.0; (d) 13.0: (e) 15.0: (f) 17.0.

the two models were developed using different approaches and different surface models, there is a remarkable resemblance between the two radiance diagrams.

3) Radiance Diagrams for Moving Source and Fixed View: In all the radiance diagrams presented thus far, surface radiance is plotted as a function of viewing angle θ_r for fixed values of the source angle θ_i. We now plot radiance diagrams for both models by varying the source angle for fixed values of the viewing angle. We will show that by considering the fixed view case, the roughness parameters of the two models can be related. This relation is later used to compare the specular lobes of the two models.

Note that when viewing angle is fixed, the term $1/\cos\theta_r$ in the specular component of the Torrance–Sparrow model (54) is constant, and the shape of the specular lobe is dependent solely on the term:

$$\exp\left(-\frac{\alpha^2}{2\sigma_\alpha^2}\right). \tag{56}$$

Since $\alpha = 0$ when $\theta_r = \theta_i$, the specular lobe is found to be symmetric with respect to the specular direction. A similar analysis is applicable to the Beckmann–Spizzichino model for rough surfaces (53). The only term that is significantly affected by variations in θ_i is the term $e^{-{\nu_{xy}}^2 T^2/4\nu_z^2\sigma_h^2}$. Further, it can be shown [1] that

$$\tan\alpha = \frac{\nu_{xy}}{\nu_z} \tag{57}$$

where, as with the slope distribution model, α is the angle between the bisector of the incident and viewing directions and the surface normal vector $\boldsymbol{n}$. Assume that $\tan\alpha_o = 2\sigma_h/T$. Then

$$\exp\left(-\frac{{\nu_{xy}}^2 T^2}{4{\nu_z}^2\sigma_h^2}\right) = \exp\left(-\frac{\tan^2\alpha}{\tan^2\alpha_o}\right). \tag{58}$$

When a rough surface is gently varying, the slopes (α) of most micro-facets are small. Therefore, tangents in (58) can be approximated by their arguments, obtaining:

$$\exp\left(-\frac{{\nu_{xy}}^2 T^2}{4{\nu_z}^2\sigma_h^2}\right) = \exp\left(-\frac{\alpha^2}{2\left(\alpha_0/\sqrt{2}\right)^2}\right). \tag{59}$$

From (59) and (56), we see that the roughness parameters of the Torrance–Sparrow and Beckmann–Spizzichino models can be related as:

$$\sigma_\alpha = \frac{\alpha_o}{\sqrt{2}} = \frac{1}{\sqrt{2}}\tan^{-1}\frac{2\sigma_h}{T}. \tag{60}$$

Fig. 15 shows radiance diagrams plotted for surfaces with different roughness values using the Beckmann–Spizzichino model (left column) and the Torrance–Sparrow model (right column). Here again, only the specular lobe component is considered. Note that these radiance diagrams differ from all of the previous ones in that radiance is plotted as a function of the source angle θ_i for fixed values of the viewing angle θ_r, rather than vice-versa. Once again we assume that $\phi_r = 0$, the geometrical attenuation factor equals unity, and the Fresnel reflection coefficient is constant. For each σ_h/T ratio in the left column, (60) is used to find σ_α for the corresponding diagram in the right column. Three important observations can be made from these radiance diagrams:

- When the source direction, viewing direction, and surface normal are coplanar, the radiance curves can be represented by Gaussian functions. This can be proved analytically by setting $\phi_r = 0$ in the specular lobe component of both models.
- The peak for each radiance curve is observed at the specular angle, i.e., $\theta_i = \theta_r$. Varying source direction, rather than viewing direction, prevents off-specular peaks from occurring. In addition, the radiance values exhibit reflection symmetry with respect to the viewer-normal plane.
- The radiance diagrams predicted by the physical optics and the geometrical optics models resemble each other strongly. Though the two models use two different surface modeling parameters (height and slope, respectively), (60) does well in relating their roughness parameters.

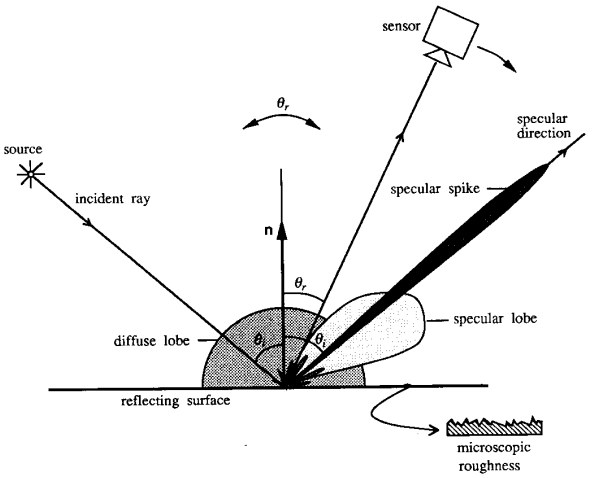

Fig. 16. Polar plots of the three reflection components as functions of the sensor direction for a fixed source direction.

B. A Unified Reflectance Framework for Machine Vision

Based on the above analysis, we propose a unified reflectance framework for machine vision. This framework describes the reflection of monochromatic light from smooth and rough surfaces. We now define the primary reflection components of the unified framework.

Primary Reflection Components: From the radiance diagrams for the Beckmann–Spizzichino and Torrance–Sparrow model, we conclude that, in general, surface radiance is comprised of three primary reflection components: the diffuse lobe, specular lobe, and specular spike. Polar plots of these three components are illustrated in Fig. 16. The components are plotted as a function of the angle of reflection (sensor direction) for a fixed angle of incidence (source direction). The radiance of the surface in the sensor direction is the sum of the three components in the sensor direction. The diffuse lobe represents the internal scattering mechanism. It is distributed around the surface normal direction. The specular lobe represents single reflection of incident light. It tends to be distributed around the specular direction and has off-specular peaks for relatively large values of surface roughness. The specular spike represents mirror-like reflection that is dominant in the case of smooth surfaces. It is concentrated in a small region around the specular direction. The magnitude of the specular lobe and specular spike components are determined by the roughness of the surface. For a very smooth surface, the specular spike component is many orders of magnitude greater than the specular lobe component. As the surface roughness increases, the spike component shrinks rapidly, and the specular lobe begins to dominate. We have seen from the radiance diagrams for the physical optics models that, for a given wavelength of incident light, the spike and lobe components are comparable to one another only for a small range of roughness values.

The Lambertian model may be used to represent the diffuse lobe component. This model has been used extensively to test shape-from-shading and photometric stereo techniques, and the

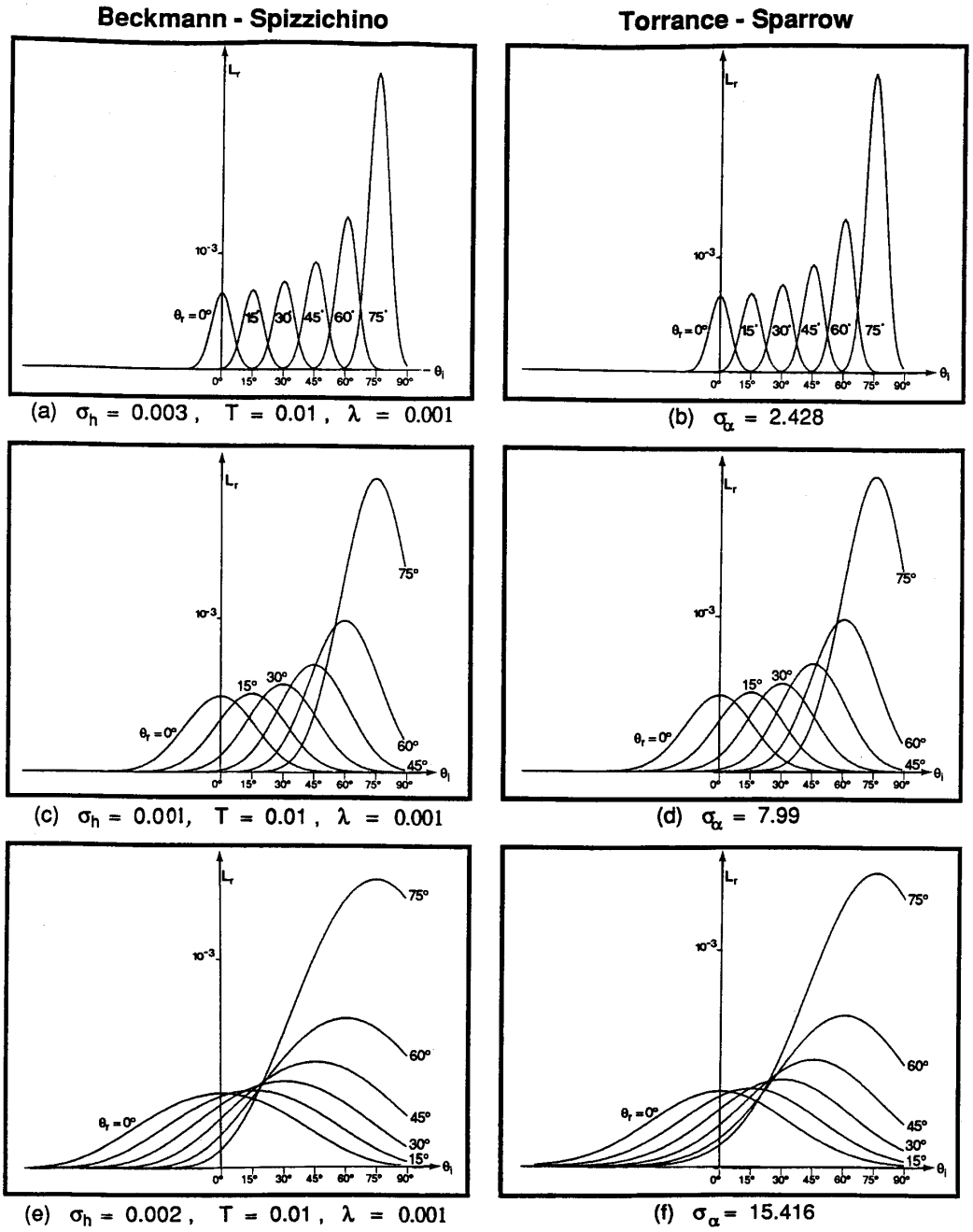

Fig. 15. Radiance diagrams for Beckmann–Spizzichino and Torrance–Sparrow models. In these diagrams, radiance is plotted as a function of θ_i for fixed values of θ_r.

results indicate that it performs reasonably well. More accurate models [18] [9] may be used at the cost of functional complexity. The specular component of the Torrance–Sparrow model can be used to approximate the specular lobe component. The Torrance–Sparrow model is simple and has been shown to conform with experimental data [38]. However, this model does not have a specular spike component. Hence, the spike component of the Beckmann–Spizzichino model may be used. We see from (52) that the shape of the spike component is determined by the term ρ_o. Since ρ_o is a very sharp function of θ_i and θ_r, the spike can be approximated by a Gaussian function with very small width or by a double-delta function. Using the above approximations, the image irradiance equation for fixed source direction and varying sensor direction can

be written as a linear combination of the three reflection components:

$$I_{im} = C_{dl} + \frac{C_{sl}}{\cos\theta_r} \exp\left(-\frac{\alpha^2}{2{\sigma_\alpha}^2}\right) + C_{ss}\delta(\theta_i - \theta_r)\delta(\phi_r) \tag{61}$$

where the constants C_{dl}, C_{sl}[8], and C_{ss} represent the strengths of the diffuse lobe, specular lobe, and specular spike components, respectively. The ratio C_{sl}/C_{ss} is dependent on the surface roughness. The radiance expression for the Beckmann–Spizzichino model (52) indicates that a closed-form relation between C_{sl} and C_{ss} is difficult to establish. However, from the radiance diagrams for the Beckmann–Spizzichino model the following assumptions can be made: $C_{sl} = 0$ when $\sigma_h/\lambda < 0.025$, and $C_{ss} = 0$ when $\sigma_h/\lambda > 1.5$. Therefore, it is only for a small range of roughness values that C_{sl} and C_{ss} are both significant.

2) Moving Source and Fixed View Representation: In the case of shape recovery methods such as photometric stereo [40], multiple measurements of the observed object are obtained by varying the source direction while keeping the sensor direction constant. We can illustrate the difference between varying source direction and varying sensor direction by introducing a new representation for the reflection components. Fig. 17 shows polar plots of the diffuse lobe, specular lobe, and specular spike. This time, however, the magnitudes of the three components of radiance in the sensor direction are determined by intersections made by the lobes with the line joining the source and the origin. In this case, the diffuse component varies with the source direction since it is proportional to the surface irradiance. Note that the specular lobe is symmetric with respect to the specular source direction $\theta_i = \theta_r$, and the spike is concentrated around the same angle. From the above observations, the image irradiance equation for fixed sensor direction and varying source direction, may be written as:

$$I_{im} = K_{dl}\cos\theta_i + K_{sl} \exp\left(-\frac{\alpha^2}{2{\sigma_\alpha}^2}\right) + K_{ss}\delta(\theta_i - \theta_r)\delta(\phi_r) \tag{62}$$

where the constants K_{dl}, K_{sl}, and K_{ss} represent the strengths of the diffuse lobe, specular lobe, and specular spike components, respectively. Once again, the ratio K_{sl}/K_{ss} is dependent on the surface roughness. K_{sl}/K_{ss} are seldom comparable in magnitude to one another. In most instances, one of the two specular components is significant while the other is negligible.

3) The Reflectance Framework and Existing Shape Recovery Methods: For a particular machine vision task, the class of surfaces involved may be known *a priori*. In such cases, the proposed reflectance framework may be used to arrive at an appropriate reflectance model for the given task. For instance, if the surfaces are homogeneous, the diffuse lobe may be ignored. If the surface roughness is small compared to the wavelength of incident light, the specular lobe component is negligible. For surfaces that are very rough, the specular spike component is nonexistent. We have provided several threshold values for the surface roughness parameters that may be used to determine which components of the reflectance framework are dominant for a given surface.

[8]We assume that θ_r is not close to the grazing angle (90°). As θ_r approaches the grazing angle, the geometrical attenuation factor rapidly approaches zero and C_{sl} is no longer a constant.

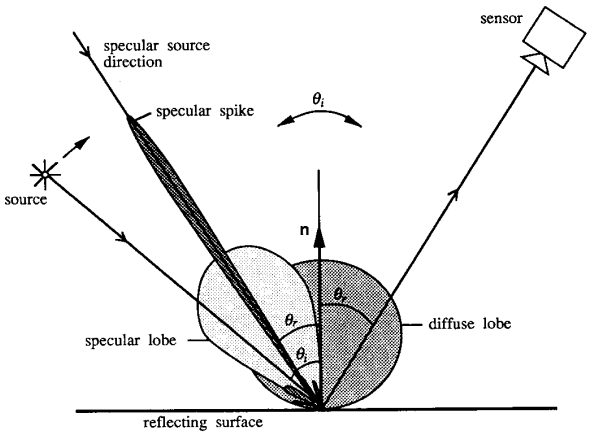

Fig. 17. Polar plots of the three reflection components as functions of the source angle for a fixed sensor direction.

Several shape recovery techniques used in machine vision are based on reflectance models that fall within the proposed framework. Shape-from-shading [15] and photometric stereo [40] [6] methods are often based on the assumption that the surface is Lambertian in reflectance. Hence, these algorithms use the diffuse lobe component and ignore the specular lobe and spike components. The specular spike model has been used to develop techniques based on photometric stereo [17] and structured highlight [29] to recover the shape of very smooth surfaces. The photometric sampling method [21] uses a combination of the diffuse lobe and the specular spike to recover the shape and reflectance of Lambertian, specular, and hybrid surfaces. The shape-from-specularity method [10] uses the specular lobe component to recover local shape of glossy surfaces. More recently, a combination of the diffuse lobe and the specular lobe has been used [36] to recover the shape and reflectance of surfaces by photometric stereo.

C. Remarks

We summarize this section with the following remarks:

- We compared the Beckmann–Spizzichino (physical optics) and Torrance–Sparrow (geometrical optics) models on the basis of their radiance diagrams. The effects of surface roughness on the radiance of the surface were studied in detail.
- We proposed a reflectance framework that has three primary components: the diffuse lobe component, the specular lobe component, and the specular spike component.
- The Lambertian model may be used to represent the diffuse lobe component. This model has been used extensively to test shape-from-shading and photometric stereo

techniques, and the results indicate that it performs reasonably well.

- The Beckmann–Spizzichino physical optics model predicts both the specular lobe and spike components. For a very smooth surface ($\sigma_h \ll \lambda$), the spike component dominates and the surface behaves like a mirror. As the roughness increases, the spike component shrinks rapidly, and the lobe component begins to dominate. The two components are simultaneously significant for only a small range of roughness values.
- A sharp specular component may result from the specular spike component when the surface is smooth ($\sigma_h/\lambda < 1.5$), and/or from the specular lobe component when the surface is gently undulating ($\sigma_h/T < 0.02$).
- The Torrance–Sparrow geometrical optics model provides a good approximation for the specular lobe component of the Beckmann–Spizzichino model. Both models are successful in predicting off-specular peaks in the specular lobe component. In view of its simpler mathematical form, the Torrance–Sparrow model may be used to represent the specular lobe component.
- The Torrance–Sparrow model is not capable of describing the mirror-like behavior of smooth surfaces and, hence, should not be used to represent the specular spike component.
- The specular lobes of both Torrance–Sparrow and Beckmann–Spizzichino models tend to have specular peaks, rather than off-specular peaks, when the viewing direction is fixed and the source direction is varied.
- Though the two models were derived using different surface modeling approaches, their roughness parameters can be related to one another by comparing the equations that describe their specular lobe components.

V. Summary

We have studied in detail reflectance models based on physical optics and geometrical optics. Assumptions made during the derivations of these models were clearly stated and discussed. By analyzing the reflectance plots predicted by physical optics and geometrical optics based models, we identified the different mechanisms involved in the reflection process. A reflectance framework was then proposed that has three primary components of reflection: diffuse lobe, specular lobe, and specular spike. This framework describes the reflection of monochromatic light from surfaces that vary from smooth to rough.

Previously, specular reflection was thought of as having a single component. This paper brings to the attention of the vision research community the existence of two components of specular reflectance: the specular lobe and specular spike components. The strengths of the two components are closely related to the physical roughness of the surface. Through our radiance diagrams, we have determined several roughness threshold values that may be used to determine when the specular spike and lobe components are significant.

We have presented two representations for the primary reflection components: one for the moving sensor and fixed source case, and the second for the moving source and fixed sensor case. The functional forms of the reflection components for the moving source case are different from those for the moving sensor case. We have shown, for instance, that the specular lobe component tends to be symmetrical with respect to the specular direction for the moving source case, while it produces off-specular peaks for the moving sensor case. Such observations regarding the distributions of the reflection components can prove useful while developing surface recovery methods.

Appendix A
Electromagnetic Waves

In the atomic theory of matter, electromagnetic effects are considered to arise from the forces exerted on each other by elementary charged particles. The elementary positive and negative particles are the proton and electron, respectively. Consider two charged particles placed in the vicinity of each other. Due to their respective charges, the particles exert a force on each other. If the particles are at rest, they experience a constant electrostatic force resulting from the *electric field* generated by them. However, if the particles have different relative velocities with respect to a common frame of reference, the force acting between them differs from the electrostatic force. This statement can be verified by simple experiments [4]. The discrepancy between the forces experienced when the particles are at rest and when they are in relative motion suggests the presence of another field, namely, the *magnetic field,* in addition to the electric field. In fact, Maxwell's equations may be interpreted as a mathematical formalization of the following physical phenomenon: Associated with a time-varying electric field is a magnetic field. Therefore, the forces experienced by a moving charge can be conveniently represented by means of electromagnetic field vectors; the *electric field intensity* $\boldsymbol{E}$ and the *magnetic field intensity* $\boldsymbol{H}$. Conversely, an electromagnetic field may be generated by applying forces and physically moving charges in some region of space. The electromagnetic field does not require a medium for its existence. Therefore, electromagnetic energy can be radiated from the space in which the charged particles are moving, to form a traveling *electromagnetic wave*. The field equations for the electromagnetic wave can be derived directly from Maxwell's equations.

Consider the light waves radiated by a point source of light. When the source is at a large distance from the point of observation, the *spherical waves* radiated by the source may be assumed to be *plane waves*, like the one shown in Fig. 18. The electric and magnetic field vectors of the plane wave may be expressed as follows:

$$\begin{aligned} \boldsymbol{E} &= E_o \boldsymbol{e} e^{-i\boldsymbol{k}\cdot\boldsymbol{r}} e^{i\omega t} \\ \boldsymbol{H} &= H_o \boldsymbol{h} e^{-i\boldsymbol{k}\cdot\boldsymbol{r}} e^{i\omega t} \end{aligned} \tag{63}$$

where $\boldsymbol{k}$ is the wave propagation vector, $\boldsymbol{r}$ is the displacement vector that determines the observation point in space, and the unit vectors $\boldsymbol{e}$ and $\boldsymbol{h}$ correspond to the directions of the electric and magnetic fields, respectively. The complex coefficients E_o and H_o represent the strengths of the electric and magnetic

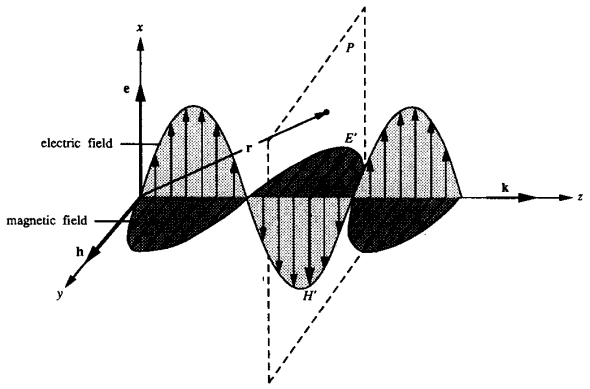

Fig. 18. An electromagnetic plane wave.

fields, respectively. It is important to note that in general the above expressions give $\boldsymbol{E}$ and $\boldsymbol{H}$ complex values. However, the actual field is determined only by the real components of the field vectors, i.e., Re[$\boldsymbol{E}$] and Re[$\boldsymbol{H}$], and the complex notation is used only for ease of mathematical manipulation.

The first exponential term in the above field equations implies that the magnitudes of electric and magnetic fields vary sinusoidally as a function of the distance along the direction of propagation. The direction of the vector $\boldsymbol{k}$ corresponds to the direction of propagation of the wave, while its magnitude k, called the *propagation constant,* determines the spatial frequency of the wave. The propogation constant is related to the wavelength λ of the plane wave as:

$$k = \frac{2\pi}{\lambda}. \tag{64}$$

If the wavelength lies between 400 and 700 nm, the wave can be detected by the human eye and is called *monochromatic light.*

The second exponential term in the field equations indicates that the field intensities also vary sinusoidally as a function of time at a radian frequency of oscillation ω. The functions that describe the spatial and temporal field variations are dependent on the function that represents the forces applied to the charged particles to generate the wave. In most engineering applications dealing with plane waves, the field is considered to be sinusoidal steady state. Using Maxwell's equations, it can be shown that the unit vectors $\boldsymbol{e}$ and $\boldsymbol{h}$ are orthogonal to each other and both these vectors are orthogonal to the propagation vector $\boldsymbol{k}$. The direction of either $\boldsymbol{e}$ or $\boldsymbol{h}$ determines the *polarization* of the plane wave. In Fig. 18, the plane wave is shown at a particular instant in time. At that instant, all points on the plane P experience the same electric and magnetic field intensities, namely, E' and H', respectively.

Since time variations in the electric field are caused by the magnetic field, and vice-versa, the amplitudes E_o and H_o of the two fields are dependent on each other, and are related as:

$$H_o = \sqrt{\frac{\varepsilon}{\mu}} E_o \tag{65}$$

where ε and μ are the *permittivity* and *permeability* of the medium, respectively. The coefficient $\sqrt{\varepsilon/\mu}$ is often referred to as the *wave impedance* of the medium. Due to the above stated dependencies between the electric and magnetic field vectors, we see that an electromagnetic wave is completely defined by either of the two field vectors, $\boldsymbol{E}$ or $\boldsymbol{H}$.

The rate of flow of *complex energy* per unit area in an electromagnetic wave can be described by a vector $\boldsymbol{S}$ called the *complex Poynting vector* [4]. $\boldsymbol{S}$ is defined as:

$$\boldsymbol{S} = \boldsymbol{E} \times \boldsymbol{H} \tag{66}$$

and the quantity

$$\boldsymbol{S}_a = \mathrm{Re}[S] = \frac{1}{2}\,\mathrm{Re}[\boldsymbol{E} \times \boldsymbol{H}*] \tag{67}$$

defines the time-averaged rate of flow of *physical energy* per unit area and has dimensions in watts per square meter. Let E, H, and S_a be the scalar values of the $\boldsymbol{E}, \boldsymbol{H}$, and $\boldsymbol{S}_a$, respectively. Then the average rate of flow of energy per unit area is determined from (67) and (65) as:

$$S_a = \frac{1}{2}\sqrt{\frac{\mu}{\varepsilon}} EE^* = \frac{1}{2}\sqrt{\frac{\varepsilon}{\mu}} HH^*. \tag{68}$$

This equation is used in Appendix C to determine the radiance of a surface from the electromagnetic field scattered by the surface.

Appendix B
Radiometric Definitions

We present definitions of radiometric terms that are used throughout this paper. Detailed derivations of these terms are given by Nicodemus *et al* [23]. Fig. 19 shows a surface element illuminated by a source of light. The *irradiance*[9] I of the surface is defined as the incident flux density (W/m^{-2}):

$$I = \frac{d\Phi_i}{dA} \tag{69}$$

where $d\Phi_i$ is the flux incident on the area dA of the surface element. The *radiance* L of the surface is defined as the flux emitted per unit foreshortened area per unit solid angle (W/m^{-2}.sr^{-1}). The surface radiance in the direction (θ_r, ϕ_r) is determined as:

$$L = \frac{d^2\Phi_r}{dA\cos\theta_r d\omega_r} \tag{70}$$

where $d^2\Phi_r$ is the flux radiated within the solid angle $d\omega_r$. The *bi-directional reflectance distribution function* (BRDF) of a surface is a measure of how bright the surface appears when viewed from one direction while it is illuminated from another direction. The BRDF is determined as:

$$f = \frac{L}{I}. \tag{71}$$

[9]The symbol E is generally used to denote irradiance [12]. In Appendix A, we have used the symbol E to denote electric field intensity. Hence, we denote irradiance by I to avoid confusion.

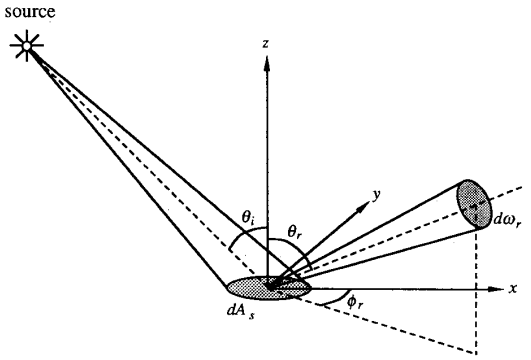

Fig. 19. Basic geometry used to define radiometric terms.

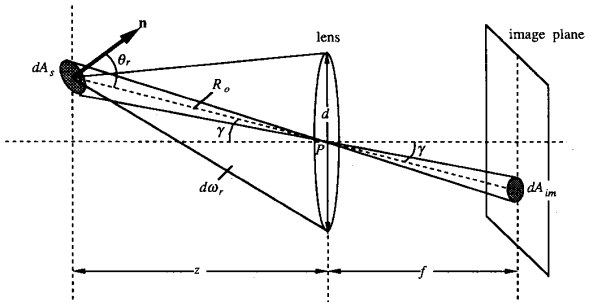

Fig. 20. Image formation: Light waves radiated by the surface area dA_s and gathered by the lens are projected onto an area dA_{im} on the image plane.

APPENDIX C
SURFACE RADIANCE FROM SCATTERED POWER

The Beckmann–Spizzichino reflectance model predicts the electromagnetic power scattered by a surface. Here, we derive an expression for the radiance of the surface from the scattered power. Surface radiance is defined in Appendix B as the flux emitted per unit foreshortened area per unit solid angle:

$$L_r = \frac{d^2\Phi_r}{d\omega_r\, dA_s \cos\theta_r}. \tag{72}$$

Consider the image formation geometry shown in Fig. 20. For convenience, we will use the areas and solid angles shown in the figure to determine surface radiance. The surface element dA_s is projected by the lens onto an area dA_{im} on the image plane. Since dA_s and dA_{im} subtend the same solid angle from the center P of the lens, they can be related as:

$$dA_s = \frac{dA_{im}\cos\gamma}{\cos\theta_r}\left(\frac{z}{f}\right)^2. \tag{73}$$

For a given sensor (e.g., CCD camera), dA_{im} is the area of the smallest sensor element (pixel). Since dA_{im} is constant for a given sensor, dA_s must be determined from dA_{im} using the above equation.

All light rays radiated by dA_s that are incident on the lens area dA_l are projected onto the image area dA_{im}. Hence, $d\omega_r$ in (72) is the solid angle subtended by the lens when viewed from dA_s:

$$d\omega_r = \frac{dA_l\cos\gamma}{R_o^2}. \tag{74}$$

The flux $d^2\Phi_r$ in (72) is the energy of light received by the lens area dA_l. It can be determined from the scattered power $<E_2E_2{}^*>$ by using (68) in Appendix A as:

$$d^2\Phi_r = S_a\, dA_l\cos_\gamma = \frac{1}{2}\sqrt{\frac{\mu}{\varepsilon}}\,<E_2E_2^*>\, dA_l\cos_\gamma. \tag{75}$$

By substituting (73), (74), and (75) into (72), we obtain:

$$L_r = \frac{1}{2}\sqrt{\frac{\mu}{\varepsilon}}\frac{R_o^2 f^2\,<E_2E_2^*>}{z^2\, dA_{im}\cos_\gamma}. \tag{76}$$

It is not possible to determine the exact value of the radiance from the statistics of the scattered power. The radiance L_r in the above equation is actually the mean (expected) radiance $<L_r>$. In the case of the Beckmann–Spizzichino model, the mean scattered power $<E_2E_2{}^*>$ (18) is determined as an integral over the entire area of the surface. In Fig. 20, we see that the sensor element dA_{im} receives light radiated only by the surface element dA_s. Hence, the mean scattered power must be computed as an integral over the surface area $A = dA_s$. Since dA_{im} is constant, A is determined by (73). Substituting the expression for $<E_2E_2{}^*>$ derived by Beckmann and Spizzichino (18) in (76), the radiance of a surface whose height h is normally distributed with mean value $<h> = 0$, standard deviation σ_h, and correlation distance T, is obtained as:

$$L_r = \sqrt{\frac{\mu}{\varepsilon}}\frac{{E_{o1}}^2\cos^2\theta_i}{2\lambda^2}\, e^{-g}\left(\left(\frac{z}{f}\right)^2\frac{dA_{im}\cos\gamma}{\cos^2\theta_r}\,\rho o^2 + \frac{\pi T^2 D^2}{\cos\theta_r}\sum_{m=1}^{m=\infty}\frac{g^m}{m!\,m}\, e^{-{\nu_{xy}}^2T^2/4m}\right). \tag{77}$$

L_r is the sum of two components: the specular spike and the specular lobe. From (77) and (73) we note that the specular spike component is proportional to the viewed area dA_s. However, it can be shown that the integral of ρo^2 is inversely proportional to dA_s. In other words, though the magnitude of the spike component is proportional to dA_s, the energy contained in the spike component is independent of it.

Radiance expressions for the special cases of smooth and rough surfaces also can be determined from the corresponding expressions for scattered power, [(23) and (24)] derived by Beckmann and Spizzichino:

$$L_{r\text{smooth}} = \sqrt{\frac{\mu}{\varepsilon}}\frac{{E_{o1}}^2\cos^2\theta_i}{2\lambda^2}\, e^{-g}\left(\left(\frac{z}{f}\right)^2\frac{dA_{im}\cos\gamma}{\cos^2\theta_r}\,\rho_o^2 + \frac{\pi T^2 D^2 g}{\cos\theta_r}\, e^{-{\nu_{xy}}^2T^2/4}\right) \qquad (g \ll 1), \tag{78}$$

$$L_{r\text{rough}} = \sqrt{\frac{\mu}{\varepsilon}}\frac{{E_{o1}}^2\cos^2\theta_i\pi T^2 D^2}{2\lambda^2\cos\theta_r{\nu_z}^2{\sigma_h}^2}\exp\left(\frac{-{\nu_{xy}}^2T^2}{4{\nu_z}^2{\sigma_h}^2}\right) \qquad (g \gg 1). \tag{79}$$

The irradiance of the surface is the light energy incident per unit area. If E_1 is the scalar value of the incident field $\boldsymbol{E_1}$ the irradiance can be obtained by once again using (68):

$$I_s = S_a \cos\theta_i = \frac{1}{2}\sqrt{\frac{\mu}{\varepsilon}} <E_1 E_1^*> \cos\theta_i \qquad (80)$$

where the term $\cos\theta_i$ accounts for the fact that the same amount of incident energy is received by a larger surface area when the angle of incidence θ_i is increased. The BRDF of the surface is determined using (77) and (80) as $f_r = L_r/I_s$.

Using the imaging geometry shown in Fig. 20, Horn [14] derived a relationship between surface radiance L_r and image irradiance I_{im}. Image irradiance is found to be proportional to surface radiance and is given by:

$$I_{im} = L_r \frac{\pi}{4}\left(\frac{d}{f}\right)^2 \cos^4\gamma. \qquad (81)$$

When the image covers only a narrow angle of the scene, $\gamma \approx 0$, and it is reasonable to assume that $\cos\gamma = 1$ in the above equations.

APPENDIX D
RELATING $d\omega'$ TO $d\omega_r$

The Torrance–Sparrow reflectance model is described in Section III-B. The reflecting surface is modeled as a large collection of planar (ideal specular) micro-facets. While deriving the radiance of the surface, (48) is used to determine the range (dw') of planar facets that reflect incident light into a given solid angle $(d\omega_r)$. Here, we derive the relation between $d\omega'$ and $d\omega_r$.

Fig. 21 shows the plane that includes the incident and reflected light rays. The light rays incident on the surface are assumed to be parallel. This assumption if valid when the source is at a large distance from the surface. Only those facets whose normal vectors lie within the solid angle $d\omega'$ can reflect light into the solid angle $d\omega_r$. The infinitesimal areas dA_r and dA_2 subtend the same solid angle from the point I. Since dA_r and dA_2 are parallel to one another and the distance $IR = 2IP$, only those facets whose normal vectors pass through dA_2 can reflect incident light into $d\omega_r$. The areas dA_r and dA_2 can be related as $dA_2 = dA_r/4$. Similarly, dA_1 and dA_2 subtend the same solid angle $(d\omega')$ from the point O. Noting that $OP = \cos\theta_i'$, the two areas can be related as $dA_1 = dA_2/\cos^2\theta_i'$. Further, the area dA' is a projection of the area dA_1 onto the unit sphere, i.e., $dA' = dA_1/\cos\theta_i'$. Further, the area dA' is a projection of the area dA_1 onto the unit sphere, i.e., $dA' = dA_1/\cos\theta_i$. Using the above equations, we can relate dA' to dA_r as $dA' = dA_r/4\cos\theta_i'$. Since $d\omega' = dA'$ and $d\omega_r = dA_r$ (areas on the unit spheres), we have:

$$d\omega' = \frac{d\omega_r}{4\cos\theta_i'}. \qquad (82)$$

Hence, for a given $d\omega_r$, the shape and size of the corresponding $d\omega'$ is dependent on the local angle of incidence θ_i', which is in turn dependent on the angle of incidence θ_i and the angles of reflectance (θ_r, ϕ_r) (38). Note that, for a perfectly smooth surface, the parallel incident rays will be reflected in a single direction (the specular direction) and will not be scattered into a cone as shown in Fig. 21. Hence, for this limiting case, the above relationship between $d\omega'$ and $d\omega_r$ is **not** valid. Consequently, the Torrance–Sparrow model is not applicable to perfectly smooth surfaces.

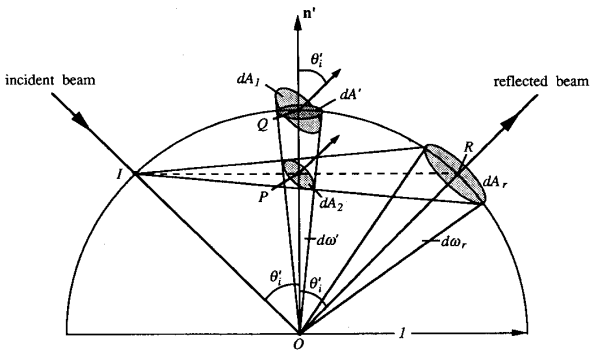

Fig. 21. The source-viewer plane used to relate $d\omega'$ and $d\omega_r$.

ACKNOWLEDGMENT

The authors thank F. Tabakin and the reviewers for their valuable comments.

REFERENCES

[1] P. Beckmann and A. Spizzochino, *The Scattering of Electromagnetic Waves from Rough Surfaces,* New York: Pergamon, 1963.
[2] J. M. Bennett and L. Mattsson, *Introduction to Surface Roughness and Scattering,* Washington, DC: Optical Soc. Amer., 1989.
[3] R. C. Birkebak and E. R. G. Eckert, "Effects of roughness of metal surfaces on angular distribution of monochromatic reflected radiation," *J. Heat Transfer,* 87, pp 85–94, Feb. 1965.
[4] E. V. Bohn, *Introduction to Electromagnetic Fields and Waves,* Reading, MA: Addison-Wesley, 1967.
[5] S. Chandrashekar, *Radiative Transfer,* New York: Dover, 1960.
[6] E. N. Coleman and R. Jain, "Obtaining 3-dimensional shape of textured and specular surface using four-source photometry," *Comput. Graphics Image Processing,* vol. 18, no. 4, pp. 309–328, Apr. 1982.
[7] R. L. Cook and K. E. Torrance, "A reflectance model for computer graphics," *ACM Comput. Graphics,* vol. 15, no. 3, pp. 307–316, 1981.
[8] H. Davies, "The reflection of electromagnetic waves from rough surfaces," *Proc. IEEE,* Pt III, vol. 101, pp. 209–214, 1954.
[9] W. G. Egan, T. Hilgeman, and J. Reichman, "Determination of absorption and scattering coefficients for nonhomogeneous media. 1: Experiment," *Appl. Opt.,* vol. 12, no. 8, pp. 1816–1823, Aug. 1973.
[10] G. Healey and T. O. Binford, "Local shape for specularity," in *Proc. Image Understanding Workshop,* vol. 2, Feb. 1987, pp. 874–887.
[11] B. K. P. Horn, "Shape from shading: A method for obtaining the shape of a smooth opaque object from one view," MIT Project MAC Int. Rep. TR-79 and MIT AI Lab. Tech. Rep. 232, Nov. 1970.
[12] B. K. P. Horn and R. W. Sjoberg, "Calculating the reflectance map," *Appl. Opt.,* vol. 18, no. 11, pp. 1770–1779, June 1979.
[13] B. K. P. Horn, "Hill shading and the reflectance map." *Proc. IEEE,* vol. 69, no. 1, pp. 14–47, Jan. 1981.
[14] ——, *Robot Vision,* Cambridge, MA: MIT Press, 1986.
[15] B. K. P. Horn, and M. J. Brooks, Eds., *Shape from Shading,* Cambridge, MA: MIT Press, 1989.
[16] A. F. Houchens and R. G. Hering, "Bidirectional reflectance of rough metal surfaces," in *Thermophysics of spacecraft and planetary bodies,* New York: G. B. Heller, Eds. Academic, 1967.
[17] K. Ikeuchi, "Determining surface orientations of specular surfaces by using the photometric stereo method," *IEEE Trans. Pattern Anal. Machine Intell.,* vol. 3, no. 6, pp. 661–669, Nov. 1981.

[18] P. Kubelka and F. Munk, "Ein Beitrag sur Optik der Farbanstriche," *Z. Phys.*, vol. 12, 593, 1931.
[19] J. H. Lambert, *Photometria sive de mensura de gratibus luminis, colorum et umbrae.*, Augsberg, Germany: Eberhard Klett, 1760.
[20] S. K. Nayar, A. C. Sanderson, L. E. Weiss, and D. D. Simon, "Specular surface inspection using structured highlight and Gaussian images," *IEEE Trans. Robotics Automat.*, vol. 6, no. 2, pp. 208–218, Apr. 1990.
[21] S. K. Nayar, K.Ikeuchi, and T. Kanade, "Determining shape and reflectance of hybrid surfaces by photometric sampling," *IEEE Trans. Robotics Automat.*, vol. 6, no. 4, pp. 418–431, Aug. 1990.
[22] ——, "Surface reflection: Physical and geometrical perspectives," *Proc. Image Understanding Workshop,* pp. 185–212, Sept. 1990.
[23] F. E. Nicodemus, J. C. Richmond, J. J. Hsia, I. W. Ginsberg, and T. Limperis, "Geometrical considerations and nomenclature for reflectance," NBS Monograph 160, National Bureau of Standards, Oct. 1977.
[24] A. P. Pentland, "Local shading analysis," *IEEE Trans. on Pattern Anal. Machine Intell.* vol. 6, no. 2, pp. 170–187, Mar. 1984.
[25] B. Phong, "Illumination for computer generated pictures," *Commun. ACM,* vol. 18, pp. 311–317, 1975.
[26] *American Institute of Physics Handbook.*, New York: McGraw-Hill, 1972.
[27] J. Reichman, "Determination of absorption and scattering coefficients for nonhomogeneous media. 1: Theory," *Appl. Opt.*, vol 12, no. 8, pp. 1811–1815, Aug. 1973.
[28] W. A. Rense, "Polarization studies of light diffusely reflected from ground and etched glass surfaces," *J. Opt. Soc. Amer.* vol. 40, no. 1, pp. 55–59, Jan. 1950.
[29] A. C. Sanderson, L. E. Weiss, and S. K. Nayar, "Structured highlight inspection of specular surfaces," *IEEE Trans. Pattern Anal. Machine Intell.* New York: vol. 10, no. 1, pp. 44–55, Jan. 1988.
[30] R. Siegel and J. R. Howell, *Thermal Radiation Heat Transfer,* New York: McGraw-Hill, 1972.
[31] W. M. Silver, "Determining shape and reflectance using multiple images," S. M. thesis, Dept. of Elec. Eng. and Comput. Sci., MIT, Cambridge, MA, June 1980.
[32] B. G. Smith, "Geometrical shadowing of a random rough surface," *IEEE Trans. on Antennas Propagat.*, vol. 15, no. 5, pp. 668–671, Sept. 1967.
[33] E. Sparrow and R. Cess, *Radiation Heat Transfer,* New York: McGraw-Hill, 1978.
[34] J. M. Stone, *Radiation and Optics,* New York: McGraw-Hill, 1963.
[35] H. D. Tagare and Rui J. P. deFigueriedo, "A framework for the construction of general reflectance maps for machine vision," Tech. Rep. Dept. of Elect. and Comput. Eng., Rice University, Houston, TX, 1988.
[36] ——, "Simultaneous estimation of shape and reflectance maps from photometric stereo," in *Proc. 3rd Int. Conf. Comput. Vision* pp. 340–343, Dec. 1988.
[37] K. Torrance and E. Sparrow, "Off-specular peaks in the directional distribution of reflected thermal radiation," *J. Heat Transfer,* pp. 223–230, May 1966.
[38] ——, "Theory for off-specular reflection from roughened surfaces," *J. Opt. Soc. Amer.*, no. 57, pp. 1105–1114, 1967.
[39] L. B. Wolff, "Spectal and polarization stereo methods using a single light source," in *Proc. Image Understanding Workshop,* vol. 2, Feb. 1987, pp. 81–820.
[40] R. J. Woodham, "Photometric stereo: A reflectance map technique for determining surface orientation from image intensity," *Proc. SPIE,* vol. 155, pp. 136–143, 1978

Shree K. Nayar (S'86–M'90) received the Ph.D. degree in electrical and computer engineering from Carnegie-Mellon University, Pittsburgh, PA, in 1990.

He is currently an Assistant Professor in the Department of Computer Science at Columbia University, New York. In the summer of 1989, he was a Visiting Research Scientist at the Production Engineering Research Laboratory, Hitachi Ltd., Yokohama, Japan. He has several patents for his inventions related to machine vision. His research interests include physical models for vision, vision sensors, and robotics.

Dr. Nayar was awarded the Marr Prize at the 1990 International Conference on Computer Vision for his paper on interreflections.

Katsushi Ikeuchi (M'89) for a photograph and biography, please see page 610 of this issue.

Takeo Kanade (M'80–SM'88) for a photograph and biography, please see page 610 of this issue.